

# Graph Transformer-Based Flood Susceptibility Mapping: Application to the French Riviera and Railway Infrastructure Under Climate Change

Vemula Sreenath<sup>1\*</sup>; Filippo Gatti<sup>1</sup>; Pierre Jehel<sup>1</sup>

<sup>1</sup>Université Paris-Saclay, CentraleSupélec, ENS Paris-Saclay, CNRS, LMPS - Laboratoire de Mécanique Paris- Saclay, 91190, Gif-sur-Yvette

\*Corresponding author: vsreenath2@gmail.com

## Abstract

Increasing flood frequency and severity due to climate change threatens infrastructure and demands improved susceptibility mapping techniques. While traditional machine learning (ML) approaches are widely used, they struggle to capture spatial dependencies and poor boundary delineation between susceptibility classes. This study introduces the first application of a graph transformer (GT) architecture for flood susceptibility mapping to the flood-prone French Riviera (e.g., 2020 Storm Alex) using topography, hydrology, geography, and environmental data. GT incorporates watershed topology using Laplacian positional encoders (PEs) and attention mechanisms. The developed GT model has an AUC-ROC (0.9739), slightly lower than XGBoost (0.9853). However, the GT model demonstrated better clustering and delineation with a higher Moran's I value (0.6119) compared to the random forest (0.5775) and XGBoost (0.5311) with p-value < 0.0001. Feature importance revealed a striking consistency across models, with elevation, slope, distance to channel, and convergence index being the critical factors. Dimensionality reduction on Laplacian PEs revealed partial clusters, indicating they could capture spatial information; however, their importance was lower than flood factors. Since climate and land use changes aggravate flood risk, susceptibility maps are developed for the 2050 year under different Representative Concentration Pathways (RCPs) and railway track vulnerability is assessed. All RCP scenarios revealed increased area across susceptibility classes, except for the very-low category. RCP 8.5 projections indicate that 17.46% of the watershed area and 54% of railway length fall within very-high susceptible zones, compared to 6.19% and 35.61%, respectively, under current conditions. The developed maps can be integrated into a multi-hazard framework.

## Keywords

Flood susceptibility; French Riviera; Graph Transformer; Explainability; Climate and LULC projections; Railway infrastructure

## Highlights

1. Developed the first flood susceptibility map for the French Riviera
2. Graph Transformer model enhances spatial autocorrelation in flood susceptibility mapping.
3. Elevation, slope, distance to channel, and convergence index dominate flood factors.
4. Spatial metrics must be additionally used to validate the accuracy of boundary delineation.
5. RCP 8.5 projects 54% of tracks in very-high susceptible zones by 2050, up from 35.61%.

6.

## 1. Introduction

Floods are the third most damaging disaster after storms and earthquakes between 1995 and 2015, according to the United Nations Office for Disaster Risk Reduction estimates. Approximately 150,000 flood events were recorded, with 157,000 lives lost, affecting 2.3 billion people and causing damages of around US \$662 billion (Ghosh et al., 2022). Flooding can result in secondary effects such as landslides, ground instability, soil erosion, scouring, and diseases such as typhoid and cholera (Rudra & Sarkar, 2023). Additionally, flooding causes annual damage of US\$14.6 billion to road and rail infrastructure globally, with 7.5% of global railway assets exposed to 1 in 100-year flood events (Koks et al., 2019). In the context of the European Union, flood-related damage to railways amounts to €581 million annually (Bubeck et al., 2019), and 25% of all the natural disaster events occurring to French railways correspond to flooding (Cheetham et al., 2016). Among railway infrastructure components, tracks are the most vulnerable to flood damage only after landslides, which are earthquake- or flood-triggered (Montoya-Araque et al., 2025). Of all natural hazards affecting railway infrastructure, 40% of the impact is caused by track flooding resulting in line closure, and 47% is related to landslides, which could be earthquake- or flood-triggered (Montoya-Araque et al., 2025). Tracks are the most vulnerable railway elements affected by flooding (Toribio Diaz & Vallhonrat Blanco, 2025). Furthermore, climate change influences flooding patterns, magnitude, and intensity, resulting in around 40% increase in flood frequency (Nguyen, 2023). Climate change and increased urban settlements, especially along rivers, will exacerbate flood damage in the coming decades. Estimates project an annual flooding loss of US\$1 trillion by 2050 (Habibi et al., 2023).

Given the disastrous effects of present and future flooding on human lives and infrastructure, one approach to mitigate risk could be to predict floods: their spatial and temporal distribution, magnitude, duration, and other details (Hong et al., 2018). However, the flooding process is challenging to predict accurately as this process is dynamic and complex (Hong et al., 2018; Bui et al., 2019). Alternatively, researchers develop a flood susceptibility map as it is an essential step that assists local authorities in risk mitigation and managing future floods (Chapi et al., 2017; Pham et al., 2020). Several flooding factors (e.g., elevation of the region, precipitation, soil type) cannot be controlled, but local authorities can prohibit constructions in highly susceptible flood areas, promote vegetation growth, construct reservoirs, and other approaches to mitigate flood risk (Ahmed et al., 2022; Widya et al., 2024).

The flood susceptibility map indicates the likelihood of an area affected by flooding using data from the watershed's topographic, meteorological, geological, and environmental characteristics (Pham et al., 2020; Nguyen, 2023). Thus, unlike flood hazard analysis, which incorporates temporal characteristics of flooding, flood susceptibility focuses only on spatial distribution. Furthermore, almost all researchers assume these variables are static (e.g., Bui et al., 2019; Ghosh et al., 2022; Pradhan et al., 2023) and assessed for present climate and land use conditions.

The French Riviera has experienced several significant floods in the past decades: the 1994 and 2010 Var floods, the 2015 Côte d'Azur flood, and the 2020 Storm Alex flood. Storm Alex, which affected multiple countries (and this region was one of them), was particularly notable, resulting in damage of €2.7 billion (Ginesta et al., 2023), with around 12 bridges collapsed (Tende, 2022). Prakash and Manconi (2021) identified over 1,249 landslides triggered by this flooding event using deep learning. Despite these devastating floods in this region, to the authors' knowledge, no previous flood susceptibility studies were published.

Modeling the hydrological process can be broadly classified into three main approaches: conceptual, physical, and empirical (Bui et al., 2019). Conceptual models are semi-empirical approaches. They calibrate model parameters using large amounts of hydrological and metrological data (Gharbi et al., 2016). Physical models such as HEC-RAS (Ongdas et al., 2020) and MIKE Flood (Tansar et al., 2020) model rainfall-runoff relationships and solve finite difference equations, but they require large amounts of data for calibration (Wang et al., 2017; Nguyen, 2023) and are only efficient in predicting the short-term duration (Nguyen, 2023); however, at regional scale data are scarce for calibration (Ahmadlou et al., 2020). Furthermore, they fail to simulate flooding for different scenarios accurately. They require considerable computational resources, especially for large watersheds (Pham et al., 2021). Empirical approaches are black-box models that use less data and produce highly predictive models (Chapi et al., 2017; Pham et al., 2021). This approach is further divided into qualitative (using expert knowledge) and quantitative approaches (using data). Analytical Hierarchy Process (Das, 2020), fuzzy logic (Akay, 2021), frequency ratio (Wang et al., 2021), logistic regression (Özay & Orhan, 2023), weights of evidence (Tehrany et al., 2014), and information value (Addis, 2023) are some of the qualitative approaches used in flood susceptibility studies. They could produce biased results and induce uncertainty due to experts' judgment and opinions (Zhao et al., 2019) and are prone to error (Khosravi et al., 2019). These simpler models fail to capture nonlinear relationships, and in recent years, data-driven machine-learning approaches have been significantly used.

Machine learning (ML) approaches can learn nonlinear patterns from the data without fully understanding the underlying process (Islam et al., 2021). Despite not modeling the entire process, these approaches can produce more accurate models than traditional approaches with fewer computational resources and reduce the need for subjective expert weights (Nguyen, 2023). Adaboost (Jahanbani et al., 2024), artificial neural network (ANN) (Bui et al., 2020), convolutional neural network (CNN) (Gao et al., 2024), decision trees (Khosravi et al., 2019; Chen et al., 2020), naïve Bayes (Chen et al., 2020; Pham et al., 2020), neuro-fuzzy (Termeh et al., 2018; Wang et al., 2019), random forest (RF) (Chen et al., 2020; Abedi et al., 2022), support vector classification (SVC) (Tehrany et al., 2014; Choubin et al., 2018), transfer learning (Zhao et al., 2021), and eXtreme Gradient Boosting (XGBoost) (Abedi et al., 2022) are some of the ML approaches used for flood susceptibility. In recent years, classical ML approaches have become less popular because of the problem of overfitting and being prone to getting stuck in the local minima, and thus, researchers have either used ensemble hybrid approaches (Tehrany et al., 2014; Choubin et al., 2018; Islam et al., 2021; Saikh & Mondal, 2023) to overcome the limitations of one or several models and/or used in conjugation with metaheuristic optimization techniques. Ant colony optimization, genetic algorithm, and swarm intelligence algorithms are commonly used metaheuristic techniques (Termeh et al., 2018; Arabameri et al., 2022). Mosavi et al. (2018) and Bentivoglio et al. (2022) provide a detailed overview of different ensemble and metaheuristic algorithms used in flood susceptibility, which are thus not discussed here.

Bentivoglio et al. (2022) highlighted from their comprehensive survey that all the models were developed for regular grids (e.g., ANN and CNN), resulting in a lack of generalization and limited exploitation of patterns in the data. They suggested a geometric learning approach as a future direction to overcome the traditional ML model limitations. Graph neural networks (GNNs) belong to this class of geometric learning in which the nodes could represent flooding factors and edges could represent flow direction or distance between two points. There are many variants in GNN architecture, such as vanilla GNN, graph attention network, and graph transformer. Vanilla GNN considers message passing to learn

the pattern from the data – each node computes messages from all its neighbors, then all the messages are aggregated, and node representations are updated based on the aggregated messages (Gilmer et al., 2017). In the case of the Graph ATtention network (GAT) (Veličković et al., 2017), attention between different edges is also considered along with message passing. However, these two architectures do not consider the global positioning of nodes in the message passing. Graph transformer (GT) (Dwivedi & Bresson, 2020) overcomes this limitation by incorporating positional encodings (PEs) into the node embeddings.

Wang et al. (2023) developed the first GAT-based flood susceptibility model using fewer inputs and obtained better performance than traditional ML approaches. Zhang et al. (2024) noted that conventional deep learning models do not work well for complex environments as they fail to capture correlations between landslide occurrence and susceptible environments accurately, and they developed a GT-based model for landslide susceptibility. They observed that the area under the curve (AUC) for the GT model is 2.05% higher than GNN and GAT models and 8.8% higher than traditional ML models. Belvederesi et al. (2025) used graph architecture to represent landslide spatial information and transformer for regression and Squared Error-Relevance Area (SERA) loss to capture landslide susceptibility accurately, and they concluded their results are promising. Despite the GT model being used for other natural hazards, it has not yet been explored for flood susceptibility.

The limited explainability of ML and ensemble models is often criticized, and researchers have attempted to improve their interpretability. Pradhan et al. (2023) were the first to research this direction to understand the importance of features using the SHapley Additive exPlanations (SHAP) (Lundberg & Lee, 2017) model. They observed that land cover and elevation are the two most important features affecting flood susceptibility. Wang et al. (2024) developed a novel residual logistic regression to achieve high accuracy and explainability at the same time. They analyzed factors dominating the prediction within high and very-high susceptibility classes and observed that distance to roads and channels were the two most influential parameters. Gao et al. (2024) used the SHAP model to explain their CNN model and observed that relative elevation is the most influential parameter. The above observations demonstrate that each watershed area behaves differently as different parameters dominate in each of them.

Limited research focused on the effects of climate change and land use and land cover (LULC) on flood susceptibility, as most research focuses on current conditions. Climate change can result in weather patterns that are reflected in increased annual precipitation, frequency of droughts and heat waves (Janizadeh et al., 2021). Rogers et al. (2025) studied the increase in future flood exposure due to climate and population changes. They attribute 21.1%, 76.8%, and the remaining 2.1% to climate, population changes, and both. Hence, urban areas are sensitive to both climate and population changes. Global warming results in increased temperature, resulting in increased water-holding capacity in the atmosphere and thus, periods of increased precipitation and drought are observed (Trenberth, 2011). Representative Concentration Pathways (RCPs) are proposed based on future greenhouse gas concentrations for different emission scenarios. RCP 2.6 (very stringent climate action), 4.5 (intermediate scenario), 6 (higher intermediate scenario), and 8.5 (minimal climate action) are widely used projection scenarios, and they correspond to an increase in mean global temperature of 1.5 – 2 °C, 2 – 3 °C, 3 – 4 °C, and 4 – 5 °C, respectively by 2100 (Meinshausen et al., 2011). Janizadeh et al. (2021) studied the effects of climate change and land use for the year 2050 for Iran under RCP 2.6 and 8.5 scenarios. They observed high and very high susceptibility classes increase by 11.55% and

7.49% for RCP 2.6 and 10.61% and 5.67% for RCP 8.5 scenarios, respectively. Mahdizadeh Gharakhanlou and Perez (2022) observed that the impact of climate change and LULC was limited in two watersheds in Canada, with a mere 2.5% increase in areas of high and very-high susceptible classes for 2050 and 2080 years for RCP 4.5. Nguyen et al. (2024) combined multiple ML models and MIKE simulations under different RCP scenarios and forecasted LULC values for 2035 and 2050 and observed a significant increase in future flood risk for high and very-high classes compared to current conditions. These works highlight the need to assess the study area's climate and LULC projections on flood susceptibility.

The following objectives are proposed based on the aforementioned literature review: develop flood susceptibility models for the French Riviera using traditional ML approaches and then evaluate the performance of the GT model compared to conventional ML models, explainability of traditional and GT models, incorporate climate and LULC projections into GT model and understand how flood susceptibility is influenced, understand regions of railway tracks which are at risk of flooding under current and future flood susceptibility as an application of the developed model.

The paper is structured as follows: Initially, flooding factors are obtained from the digital elevation model (DEM) and other sources, and traditional ML models (ANN, SVC, RF, and XGBoost) are trained for the considered watershed and susceptibility maps are developed. Feature importance is studied for some models to identify key contributing factors. GT architecture is introduced, detailing how it incorporates spatial features using positional encoders, and then it is implemented. A Moran I statistical analysis evaluates whether the developed models learn spatial autocorrelations. Further, latent variable representations and feature importance ranking of the GT model are explored. The study then obtains predictions for future scenarios by incorporating climate and LULC projections for different RCP scenarios and generating flood susceptibility for each using the GT model. Throughout the study, the railway structure vulnerability is assessed by calculating the length of the railway track in each susceptibility class for current and future conditions. Finally, the manuscript concludes with some closing remarks.

## 2. Materials and Methods

### 2.1 Study Area Description

The considered watershed corresponds to Alpes de Haute-Provence, Alpes-Maritimes, and Var departments in the French Riviera (southeast of France), with geographical extents from 6°45' to 7°53' east and 43°36' to 43°94' north as shown in Fig. 1. The watershed comprises catchments from the Var, Paillon, Siagne, and Argens rivers, with a total area of around 2650 km<sup>2</sup>. The Alps mountains are to the north of the watershed, the Mediterranean Sea on the south, and Italy on the east. The mean annual precipitation in the watershed is 800 mm, distributed throughout the year; October and November are the peak seasons and July and August are the lowest precipitation. Flood inundation map is obtained from the publicly available catalogue interministériel de données (IDE) géographiques. The total inundation area is observed to be 172.6 km<sup>2</sup> (6.5% of the watershed area). Hydraulic modeling, satellite and aerial images, field observations, and other techniques were used to derive this inundation database. These values are used as the target variables in training the model.

Fig. 2 shows the railway track in the considered watershed, which has a length of around 283 km. It can be observed that it runs along the coast, with most of its length located within the inundated area (around 97 km or 35%). The national rail network track shapefile is obtained from the France railway website<sup>1</sup>.

## 2.2 Sampling Methodology

An equal number of flooded and non-flooded points are to be considered to create an unbiased dataset for training (Zhao et al., 2019). Hence, to train the ML models such as ANN, SVC, RF, and XGBoost, 1247 points are considered from the flooded and 1247 from the non-flooded dataset. Of these points, 70%, 15%, and 15% of the combined (flooded and non-flooded) datasets are used to train, validate, and test the ANN model, respectively. In contrast, 80% for training and 20% for testing from the combined dataset are used for SVC, RF, and XGBoost models with 5-fold cross-validation. 811 points (65% from each set) from flooded and non-flooded sets were considered in the case of the GT model to reduce the computational cost. From these points, 70%, 15%, and 15% points are considered for training, validation, and testing sets, respectively, and are shown in Fig. 2. This is a binary classification problem with values either flooded or non-flooded with values assigned as 1 and 0, respectively.

## 2.3 Flood Conditioning Factors

Identifying the flood conditioning factors is a crucial step in flood susceptibility study, as there are no standard guidelines for selecting them. However, after surveying previous studies, input variables from four categories are considered: topographic, hydrological, geological, and environmental.

### 2.3.1 Topographic Factors

Topography describes the watershed's physical shape, significantly impacts flooding patterns, and influences runoff, indirectly affecting precipitation (Bui et al., 2020; Islam et al., 2021). A 25m resolution DEM is obtained from the publicly available BD Alti, a government geosciences agency<sup>2</sup> for the considered departments. All the topographic factors are computed from the DEM model.

Elevation is an important factor directly affecting flooding and is inversely related. Lower areas are more prone to flooding than elevated areas, as water accumulates at lower elevations from the higher elevations (Islam et al., 2021). Consequently, coastal regions are more prone to flooding in the considered watershed. Fig. 3(a) shows the elevation levels of the considered area. It can be observed that the Alps Mountain ranges in the north and east have higher elevations with a peak value of 1845 m and relatively flat terrain along the coast.

The slope is another critical factor that directly affects flooding. Steeper slopes have increased runoff velocity and lower infiltration capacity, resulting in water accumulation downstream of the channel at gentle slopes (Nguyen, 2023). Fig. 3(b) shows slope values ranging from 0 to 1.31 radians (= 75°) with a mean value of around 12°. Gentle slopes are observed to be near the coast, and steeper slopes are in the inland mountainous regions.

---

<sup>1</sup> (<https://ressources.data.sncf.com/explore/dataset/fichier-de-formes-des-voies-du-reseau-ferre-national/export/>) (last accessed on 30 September 2024)

<sup>2</sup> <https://geoservices.ign.fr/bdalti> (last accessed on 30 September 2024)

Aspect is the slope direction, affecting flooding indirectly (Rudra & Sarkar, 2023). As the considered watershed is in the northern hemisphere, south-facing slopes are significantly more exposed to the sun than north-facing slopes, creating a local climate variation resulting in the north-facing slopes being cooler with more moisture retention than the south-facing slopes (Nguyen, 2023). Aspects affect vegetation growth, infiltration rate, and other aspects that affect flooding indirectly, and their values vary between  $0^\circ$  and  $360^\circ$ . Fig. 3(c) shows the aspect values from  $0^\circ$  to  $360^\circ$  ( $=2\pi$ ) with north, east, south, and east facing meaning,  $0^\circ$ ,  $90^\circ$ ,  $180^\circ$ , and  $270^\circ$ , respectively. Terrain has many values close to  $180^\circ$  (south-facing slopes) with less moisture retention, resulting in quicker runoff.

Curvature is the second derivative of the elevation, and plan and profile curvatures are the perpendicular and parallel directions of the curvature, respectively (Ghosh et al., 2022). Negative values of plan curvature signify convergent areas which are prone to flooding. In contrast, positive values signify divergent values and are less likely to flood. Values close to zero imply a flat terrain, and curvature cannot explain the flooding pattern, and other factors determine the flooding pattern. Fig. 3(d) shows the plan curvature of the watershed, and it can be observed that most of the values are close to zero (profile curvature values are also close to zero and were not plotted), implying limited curvature effects. The convergence index resembles plan curvature measuring water convergence (Habibi et al., 2023), as shown in Fig. 3(e).

Flow accumulation represents the total upstream cells that drain at each cell in the watershed and depends on the flow direction at each cell (Saikh & Mondal, 2023). Higher values of flow accumulation indicate that they are more susceptible to flooding. Fig. S1(a) (supplementary) shows the flow accumulation plot with a maximum value of about 17,500. Topographic wetness index (TWI) is a proxy for flood inundation regions in the watershed, with higher TWI values implying higher flooding (Rudra & Sarkar, 2023), and it describes moisture in the soil and soil erodibility (Nguyen et al., 2024) with values ranging from 8.5 to 19.2 (Fig. S1(b) supplementary). It is calculated using  $TWI = \ln (As / \tan \beta)$ . Here,  $As$  is the specific catchment area ( $m^2/m$ ) obtained from flow accumulation and  $\beta$  is the slope angle in radians (Pham et al., 2021). The topographic roughness index (TRI) is another important parameter influencing flooding, which measures unevenness or roughness in the terrain (Rudra & Sarkar, 2023). Its values range from 0 to 121 (Fig. S1(c) supplementary), with lower values implying a high probability of flooding (Islam et al., 2021). The topographic position index (TPI) represents the elevation difference of each cell with the mean of neighboring cells (Saikh & Mondal, 2023). Negative, positive, and zero TPI values imply valley, ridge, and flat regions. TPI values are dependent on the neighborhood cell size. From Fig. 3(f), most TPI values are close to zero, ranging from -53 to 45. The sediment transport index measures channel bed depth, sediment movement, and erosive capacity of the stream. It is calculated as  $STI = (As / 22.13)^{0.6} \times (\sin \beta / 0.0896)^{1.3}$  (Pham et al., 2021). Here,  $As$  and  $\beta$  were previously defined, with values ranging from 0 to 6,324 for the watershed (Fig. S1(d) supplementary). The slope length factor incorporates slope length and slope, with a higher slope length indicating more water accumulated downstream (Widya et al., 2024). For the considered watershed, these values range from 0 to 80.7 (Fig. 3(g)). Stream power index (SPI) is another critical parameter that captures the erosive power of the channel using the catchment area and slope, defined as  $SPI = As \times \tan \beta$  (Tehrany et al., 2019). Higher SPI values imply significant water accumulation and a steeper slope. The maximum SPI value for the watershed is 622,696, as shown in Fig. 3(h).

### 2.3.2 Hydrological Factors

Hydrological factors describe water flow, distribution, and quantity in the terrain. Initially, channel networks are derived from the DEM, which is used for the subsequent analysis. Drainage density positively correlates with flooding and describes the physical characteristics of the basin (Gharakhanlou & Perez, 2023). It is calculated using a moving window convolution approach with a neighborhood of 5km and an output resolution of 50m. Fig. 3(i) displays the drainage density for the watershed with a maximum value of 0.41 km/km<sup>2</sup>.

Distance to the channel is a crucial factor affecting the amount of saturation and flooding (Saikh & Mondal, 2023). Regions closer to the channel are more prone to flooding, and farther distances are less prone to flooding (Islam et al., 2021). It is calculated as the Euclidian distance from the DEM to the nearest point on the derived channel network and is shown in Fig. 3(j) with a maximum distance of around 6,333 m. Similarly, distance to coast and rail are calculated and are shown in Fig. S1(e) and Fig. S1(f) (supplementary), respectively. These plots are highly correlated since most of the track runs along the coast. Road data for the watershed is obtained from the Open Street Map. Roads are impervious, so areas near them have increased runoff and disrupted drainage patterns (Saikh & Mondal, 2023). Euclidian distance from DEM to roads is calculated as shown in Fig. 3(k). A dense road network is evident near the coasts, and a coarser network is apparent in the inland mountainous areas with a maximum value of 937 m.

Precipitation is another major factor affecting flooding, as large amounts of precipitation observed during Storm Alex could cause significant flooding (Islam et al., 2021). Monthly precipitation data is obtained from the Météo-France website from January 1994 to September 2024<sup>3</sup>. Mean annual precipitation is computed from this data and then interpolated using the ordinary kriging method shown in Fig. 3(l). The minimum and maximum precipitation values of 652 mm and 943 mm are observed, respectively, with peak values in the inland mountainous regions and lower values along the coast. Precipitation interacts with elevation, slope, and proximity to the channel, which control water accumulation, runoff velocity and infiltration rates, and river exposure, respectively, and the runoff water could only cause flooding. So, precipitation in a region does not directly translate into flooding.

### 2.3.3 Environmental Factors

Environmental factors describe the impact of natural or human modifications affecting flooding. LULC and various normalized difference indices are considered environmental factors. Fig. 3(m) shows a 10m resolution LULC raster map obtained from Karra et al. (2021). Permanent water bodies, trees (15 feet or taller) and dense vegetation, seasonally or all year-round flooded vegetation, crops and agricultural land, built areas (e.g., roads, railways, buildings), bare ground (areas with no vegetation), and rangeland are the classification categories present in the LULC. Each land cover category affects flooding differently (Rudra & Sarkar, 2023). As discussed in the introduction, increasing urbanization and land use changes affect flooding significantly, especially in urban areas. Hence, it is an essential parameter that must be considered to understand its effect on current and future flooding. Areas in the vicinity of downstream water bodies are prone to flooding. Tall trees and dense vegetation significantly reduce water velocity and increase infiltration, resulting in decreased flooding. Most watershed areas correspond to trees and rangeland categories, especially in the inland Alps mountainous regions. Built areas create artificial barriers preventing infiltration and increasing runoff and flooding. Built areas are

---

<sup>3</sup> <https://meteo.data.gouv.fr/datasets/6569b3d7d193b4daf2b43edc>, (last accessed on 15 October 2024)

mainly concentrated along coasts where cities such as Nice and Cannes are present. Low-lying, flat, bare-ground regions significantly contribute to flooding as they have no vegetation to break water velocity. Bare grounds are present in the vicinity of the built areas.

Apart from the land cover parameter, several Normalized Difference Indices, such as vegetation index (NDVI), built-up index (NDBI), and water index (NDWI), are considered. They are computed in the Google Earth Engine (GEE) using Sentinel-2 data with a cloud threshold of 10%. NDVI measures vegetation cover, making it a valuable parameter to track after flooding. It is calculated as  $NDVI = (B8 - B4)/(B8 + B4)$ . Higher NDVI values correspond to regions with higher vegetation and water infiltration, resulting in a decreased probability of flooding (Saikh & Mondal, 2023). NDWI is effective at detecting water bodies. However, it struggles to accurately detect inundated areas, as it fails to account for water under vegetation and is calculated as  $NDWI = (B3 - B8)/(B3 + B8)$  (Khalifeh Soltanian et al., 2019). NDBI uses built-up areas to detect flood-prone areas and is calculated as  $NDBI = (B11 - B8)/(B11 + B8)$ . These built areas act as impermeable surfaces, affecting permeability and increasing runoff (Nguyen, 2023). Negative values of NDBI correspond to water bodies, resulting in an inverse relation with flooding, and are especially useful in urban flooding. Most of the inundated areas (Fig. 1) are in the vicinity of urban areas (Fig. 3(m)), making NDBI an ideal candidate for understanding flooding. It can be observed that all the indices range between -1 and 1. Maximum and mean values of the past 5 years (till 25 September 2024) are computed for these indices to understand which effectively correlate with flood susceptibility. Fig. 3(n) shows a 5-year maximum NDBI value with values ranging from -0.3 to 0.9.

#### 2.3.4 Geological Factors

Finally, the geological factors describe the soil characteristics of the watershed, and they influence infiltration capacity. Lithology and soil types are considered as flooding factors. Lithology describes the geological rock formation affecting flooding as geological composition interacts and modifies permeability. Lithologies such as limestone and sandstone deposits have good permeability; hence, geology with these compositions has higher permeability and might reduce flooding (Widya et al., 2024). On the other hand, lithologies such as granite and clay have low permeability; hence, geology with these compositions has lower permeability and increased runoff. The lithology of the watershed is obtained from Pawlewicz et al. (2003) and is plotted in Fig. 3(o). J (Jurassic), K (Cretaceous), N (Neogene), P (Permian), Pg (Paleogene), Pzi (Paleozoic intrusive igneous), Pzm (Paleozoic metamorphic), PzpCmm (Paleozoic through Precambrian metamorphic), Sea1, Sea2, Tr (Triassic), Tv (Tertiary volcanic) categories are present in the watershed. The Jurassic type (where the Var catchment is located) is dominant in the watershed and typically includes sandstone and limestone composition, which are permeable.

Soil classification describes different soil types available in the region, which primarily control water infiltration capacity, significantly affecting runoff and flooding (Islam et al., 2021). Consequently, infiltration and flooding are inversely related. The soil type data for the watershed is obtained from the harmonized world soil database (FAO & IIASA, 2023) with a 1 km resolution, as shown in Fig. 3(p). The following soil types are present: Mollic Leptosols, Technosols, Open Water, Calcaric Fluvisols, Rendzic Leptosols, Umbric Leptosols, Calcaric Cambisols, and Eutric Cambisols with Rendzic Leptosols and Calcaric Cambisols dominate the watershed.

#### 2.4 Multi-Collinearity Analysis

After obtaining the above topographic, hydrological, environmental, and geological inputs, it is essential to consider independent factors for training the ML model to get unbiased results (Habibi et al., 2023). Variance inflation factor (VIF) and tolerance (TOL) are widely used approaches to quantify linear correlations for all the inputs, with high VIF values indicating high multi-collinearity (e.g., Gao et al., 2024; Bui et al., 2019). VIF is computed using the inbuilt function from the *statsmodels* library (Seabold & Perktold, 2010), and TOL is computed as  $TOL = 1/VIF$ .  $VIF < 10$  and  $TOL > 0.1$  criteria are considered for the multi-collinearity. Table S1 shows the obtained VIF and TOL values with many variables collinear. When pairwise correlation correlations (R) are considered, it is observed that elevation and precipitation are highly correlated ( $R = 0.835$ ), agreeing with the previous observation that maximum precipitation occurred in the inland and minimum precipitation in the flat regions. Slope and TRI ( $R = 0.958$ ), slope and TWI ( $R = -0.805$ ), slope and STI ( $R = 0.873$ ), TPI and profile curvature ( $R = 0.813$ ), TRI and STI ( $R = 0.847$ ), STI and SPI ( $R = 0.913$ ), distance to rail and coast ( $R = 0.912$ ), distance to coast and precipitation ( $R = 0.802$ ), NDBI mean and NDVI mean ( $R = -0.815$ ), NDVI mean and NDVI max ( $R = 0.941$ ), NDVI mean and NWDI mean ( $R = -0.968$ ), and NDVI max and NDWI mean ( $R = -0.894$ ) are highly correlated. After removing highly correlated factors, the final flooding factors considered are shown in Table 1. It should be noted that despite precipitation and elevation strongly correlated with  $VIF > 10$  and  $TOL < 0.1$ , precipitation is still considered as an input variable. One of the objectives of the current study is to understand the effect of climate projections on flood susceptibility, and its effects are incorporated through forecasted precipitation values.

### 3 Machine Learning Models

#### 3.1 Model Details

This section briefly overviews ML models: ANN, SVC, RF, and XGBoost. ANNs consist of hidden layers that are fully connected, and the model weights are trained using a backpropagation algorithm by iteratively minimizing the loss function. SVC (Cortes & Vapnik, 1995) identifies an optimal hyperplane by maximizing the margin between classes from feature space. RF (Breiman, 2001) and XGBoost (Chen & Guestrin, 2016) belong to the class of decision trees. RF constructs a parallel ensemble of decision trees using bootstrapping and aggregates the predictions using majority voting, thus reducing overfitting and improving generalization. XGBoost, on the other hand, is a sequential model that uses a gradient-boosting framework that iteratively builds trees to minimize residuals from previous trees and incorporates regularization techniques to prevent model overfitting.

The inputs and target are normalized using min-max scaling. *Optuna* library (Akiba et al., 2019), an efficient framework designed for optimizing hyperparameters of ML models, was used for hyperparameter optimization. A subset of input features determined from the hyperparameter optimization is used to train the models because the model performance did not deteriorate when fewer inputs were used. The model predictions range from 0 to 1; if they are above 0.5, they are classified as flooded; otherwise, they are non-flooded. ANN model was trained using the *Pytorch* library (Paszke et al., 2019), SVC and RF models were trained using the *Scikit-learn* (Pedregosa et al., 2011) library and XGBoost using the *XGBoost* (Chen & Guestrin, 2016) library. Table S2 details the model architecture and input features considered for each model. It should be noted that no constraint was enforced to include precipitation and LULC as inputs, as these models are not used for future forecast predictions.

### 3.2 Performance Metrics

The following binary statistical metrics are used to assess the model performance as the flood susceptibility task is a classification problem: Area Under the Receiver Operating Characteristic Curve (AUC-ROC), sensitivity (true positive rate) (Eq. 1), specificity (true negative rate) (Eq. 2), Positive Predictive Value (PPV) (Eq. 3), and Negative Predictive Value (NPV) (Eq. 4). In Eq. 1 to 4, TP, TN, FP, FN correspond to true positive, true negative, false positive, and false negative, respectively. Sensitivity and specificity are probabilities and measure the model's ability to correctly identify true positives (i.e., flooded regions) and true negatives (i.e., non-flooded regions), respectively. PPV and NPV indicate conditional probabilities: the probability that an area predicted as flood-susceptible is indeed flood-susceptible and non-flood-susceptible is indeed non-flood-susceptible, respectively (Habibi et al., 2023; Saikh & Mondal, 2023; Pradhan et al., 2023). ROC is a probability curve with 1 – specificity (false positive rate) on the X-axis and sensitivity on the Y-axis. AUC represents the probability that the model will rank positive over negative samples (Wang et al., 2023). In general, AUC values range from 0.5 to 1, with a value of 1 implying that the classifier accurately predicts flooded regions as flooded and non-flooded areas as non-flooded. Conversely, an AUC value of 0.5 indicates performance like a random guess. Higher values of the considered metrics imply better model performance.

$$\text{Sensitivity} = \frac{TP}{TP + FN} \quad (1)$$

$$\text{Specificity} = \frac{TN}{FP + TN} \quad (2)$$

$$\text{PPV} = \frac{TP}{TP + FP} \quad (3)$$

$$\text{NPV} = \frac{TN}{TN + FN} \quad (4)$$

### 3.3 Model Explainability

Interpretability and explainability are commonly used to understand how the model predicts (Rudin, 2019). Interpretable models are transparent, allowing humans to understand their reasoning and predictions without additional tools (e.g., logistic regression and decision trees). On the other hand, explainable models require additional tools (e.g., SHAP) to understand the “black box” model, which humans cannot understand inherently (Pradhan et al., 2023). Rudin (2019) argued against using explainable models (or so-called statistics summaries) as they cannot represent the original black-box model perfectly, but the ideal scenario should be developing the interpretable ML models and acknowledging significant technical challenges in developing interpretable models. In explainable ML, there are two major approaches: global feature importance (e.g., using permutation) and local importance (e.g., SHAP). In the context of permutation (Fisher et al., 2019), an input feature is randomly permuted, and its effect on prediction is observed. The higher the change in model performance, the more important the input feature modified is. Though it is simpler to implement, it cannot tell anything about an individual prediction, whether an input feature positively or negatively affects the prediction or dependency on features, but only for the generalized overall predictions.

SHAP provides a local explanation methodology using cooperative game theory (Shapley values) that attributes fair credit to each input feature based on their contribution to the model prediction. SHAP formulates the explanation as a linear model (Eq. 5) with Shapley values, considering all possible feature combinations and measuring each feature's marginal contribution. SHAP values satisfy four properties: efficiency (Shapley values sum to the difference between the actual and average predictions), symmetry (players with equal marginal contribution have the same score), the null player (player with zero marginal contribution results in zero reward), additivity (two individual games can be added to obtain overall contribution). This approach has significant advantages: local accuracy, missingness, consistency, and model-agnostic approximation (Lundberg & Lee, 2017); however, its computation cost is expensive.

$$g(z) = \phi_0 + \sum_{i=1}^M \phi_i z_i' \quad (5)$$

In Eq. 5,  $z' \in [0,1]^M$ , M is the total coalition size,  $\phi_i$  is the Shapely value.

### 3.4 Results and Discussion

This section discusses the results of the developed ML models. Table 2 shows the ML models' performance metrics for the test dataset. XGBoost achieved the highest performance across all metrics compared to other models with an AUC-ROC of 0.9853, demonstrating exceptional ability to discriminate between flooded and non-flooded classes. RF model exhibits strong performance that closely follows XGBoost. However, the highest sensitivity and specificity in the case of XGBoost imply that it predicts fewer false positives and negatives when predicting. SVC performs adequately but falls short compared to ensemble decision tree approaches such as XGBoost and RF, suggesting kernel-based approaches might struggle with high dimensional complex geospatial data. ANN significantly struggles to perform well compared to the remaining models. It achieved a modest AUC-ROC of 0.915, possibly due to limited training data size and necessitating a shallow feedforward network, which consequently struggles to learn flooded and non-flooded boundaries. Training the ANN with a metaheuristic optimizer (e.g., genetic algorithm) might improve the model performance (Islam et al., 2021).

Discrete model predictions are rasterized using the Kriging approach, and the predictions are grouped into five classes using the Jenks natural break approach (Chapi et al., 2017). It divides data into required groups by minimizing the variance within a group but maximizing the variance between groups. All the models have break values close, but for uniformity in comparison, GT model break ranges are used for all the models. The break values are: 0 - 0.0963, 0.0963 - 0.258, 0.258 - 0.456, 0.456 - 0.7, and 0.7 - 1 for very-low (cream color), low (tan color), moderate (green color), high (salmon color), and very-high (red color) classes, respectively. Additionally, values higher than 0.5 were considered flooded during the training. Consequently, high and very-high classes should ideally correspond to flooded regions, as the class break for moderate and high is around 0.456. Fig. S2, Fig. S3 (supplementary), Fig. 4, and Fig. 5 plot the flood susceptibility using the ANN, SVC, RF, and XGBoost model predictions and qualitative predictions are made using them. Additionally, Table 3 shows the area of each susceptibility class for all the models.

It can be observed from Fig. S2 and Table 3 that the ANN model shows a good correlation between the channel networks and high and very-high susceptibility regions. It also captures topographic effects with high susceptibility regions in the lowland (near coasts) and low susceptibility in the mountainous areas. However, it fails to capture very-high susceptibility in the Var catchment and instead predicts high susceptibility. It predicts larger areas of moderate susceptibility in the Siagne catchment with blurred boundaries, failing to capture sharp transitions in flood risk. It also fails to predict very-high susceptibility in critical regions like the Var, Paillon, and Siagne catchments; instead, it only predicts high susceptibility. Furthermore, it likely overestimates the track section susceptible to flooding as it predicts that 72.85% of track length falls within high and very-high susceptibility zones, significantly above the actual 35%. This conclusion aligns well with Bentivoglio et al. (2022) discussion that convolution layers incorporate inductive bias and fully connected layers struggle to capture spatial correlations.

From Fig. S3 (supplementary), it can be observed that SVC shows better transitions and spatial accuracy between susceptibility zones than ANN predictions (e.g., Siagne Catchment). Regions classified as moderate are classified as low susceptibility by the SVC in the Siagne and Argens catchments. However, it slightly overpredicts the low susceptibility region and fails to accurately identify very high susceptible regions in the Var catchment. Generalized boundaries are still evident, especially when transitioning from low to very-low susceptibility regions. Around 51% of the track length is estimated to be in high and very-high susceptibility regions.

RF model captures the transition from very-high to moderate to very-low susceptibility as we move away from channel networks in the Argens catchment, implying a better delineation of different regions than ANN and SVC, as shown in Fig. 4. This model identifies very-high susceptibility regions significantly better than previous models in all the catchments, though it fails to identify sharp boundaries precisely. High and very-high susceptible region areas add up to around 15.3%. However, track length susceptible to flooding is slightly overestimated as the combined length of high and very-high regions exceeds 63%.

XGBoost predictions are shown in Fig. 5, and despite its significantly higher AUC and other metrics, it struggles to predict very high susceptibility in the Var and Paillon catchments but instead predicts high susceptibility because the predictions above 0.5 are treated as flooded regions and are not reflected in metrics. It significantly overpredicts low susceptibility regions (67% area) and underpredicts very low susceptibility (1% area) regions because the predictions below 0.5 are treated as non-flooded regions and are not reflected in metrics. Like SVC, it struggles to identify boundaries in the Argens and Siagne catchments precisely and predicts low susceptibility in the Argens catchment and moderate susceptibility in the Siagne catchment. XGBoost struggles to capture sharp boundaries precisely. Since it underestimates the very-high susceptibility region, it is reflected in the length of the track corresponding to this region. To conclude, despite XGBoost's best performance in binary classification, it struggles significantly to differentiate between classes in flood susceptibility, and the metrics (e.g., AUC-ROC) poorly capture this.

Additionally, the SHAP plots of RF and XGBoost models are plotted (Fig. S4 supplementary) to determine the importance of features that influenced model predictions. It can be observed that topographic features such as slope, elevation, convergence index, and distance to channel (hydrological feature) are the most influential features in the RF model for predicting flooded and non-

flooded classes. Whereas similar features in different order are predicted in the case of the XGBoost model, indicating that the models have learned meaningful features to predict flood susceptibility. The SHAP values vary between -0.15 and 0.15 for the RF model (since magnitude is plotted, negative values are not evident) and -0.4 and 0.4. Additionally, SHAP values of influential features in the XGBoost are significantly high (e.g., elevation  $\approx 0.4$ , slope  $\approx 0.35$ ), and the remaining features have minimal influence, which might be why XGBoost struggles with boundary delineation despite achieving the highest accuracy, i.e., overdependence on a few features.

As discussed above, standard binary metrics fail to capture how well a model delineates spatial boundaries between different classes but provide overall model performance, and almost all the literature identifies model performance using them (and other binary classification metrics). In this regard, Moran's I test (Moran, 1950) is performed to quantify the degree of spatial autocorrelation to understand whether similar susceptibility values cluster together spatially or dispersed or in a random pattern. Fenglin et al. (2023) research was one of the few works that considered this test on model residuals to validate no spatial autocorrelation and choose the best-fit one. Gharakhanlou and Perez (2022) used this test to determine flooded and non-flooded points. However, this test is used in the present work to understand whether spatial autocorrelations are captured in the model predictions. A spatial weight matrix is constructed using a distance threshold (1000 m) criterion. Moran's I value ranges between -1 to 1. Moran's I value below  $E(I)$  (Eq. 7) implies a negative autocorrelation (dispersion) with a value of -1, implying perfect dispersion. Similarly, its value above  $E(I)$  indicates a positive autocorrelation (clustering), with a value of 1 implying a perfect clustering. Its value close to  $E(I)$  implies randomness.

$$I = \frac{n \sum_i \sum_j w_{ij} (Y_i - \bar{Y})(Y_j - \bar{Y})}{\sum_{i \neq j} \sum_j w_{ij} (Y_i - \bar{Y})} \quad (6)$$

$$E(I) = \frac{-1}{n-1} \quad (7)$$

$$z_i = \frac{Y_i - \bar{Y}}{\sigma(Y)} \quad (8)$$

$$y_i = \sum_j w_{ij} \cdot z_j \quad (9)$$

In Eq. 6, 8, and 9,  $Y_i$  is the susceptibility value for location  $i$ ,  $\bar{Y}$  is the mean of all values,  $w_{ij}$  is the spatial weights between locations  $i$  and  $j$ ,  $z_i$  is the standardized susceptibility value,  $y_i$  is the spatially lagged value, and  $E(I)$  represents the expected value of Moran's I under the null hypothesis of no spatial autocorrelation. Fig. S5 and Fig. S6 (supplementary) display the plots of XGBoost (Moran's I value = 0.5311, Z-score = 138.2673) and RF (Moran's I value = 0.5775, Z-score = 151.5387) models, respectively, with susceptibility map on the left (in Lambert 93 coordinates) and scatterplot on the right. The test results show significant statistical significance with p-value < 0.0001, and the z-score quantifying statistical significance of observed spatial autocorrelation is significantly above 1.96 for 95% statistical levels. As discussed above, a higher Moran's I value implies a tighter clustering, and since the RF model has a higher Moran's I value and Z-score, it exhibits better spatial autocorrelations, resulting in better

transitions from one susceptible class to another (which was concluded in the susceptibility plots as well). A higher scatter in the spatially lagged values in the case of the moderate and high susceptibility classes for the XGBoost model indicates that points from similar classes are less surrounded by points in these classes. Additionally, comparing high standardized values (above 1) and high spatially lagged values (above 1.5) of both these plots, it is evident that other high and very-high susceptibility areas consistently surround high and very-high susceptibility locations. In the next section, GT architecture and its implementation are discussed.

#### 4. Graph Transformer Model

To our knowledge, no transformer architecture (Vaswani et al., 2017) has been applied to the graph structure known as graph transformer (Dwivedi & Bresson, 2020) for the flood susceptibility problem; our idea with this manuscript is to create a blueprint that others could easily replicate to other regions with regional modifications.

##### 4.1 Graph Transformer Architecture

The transformer architecture (Vaswani et al., 2017) developed at Google fundamentally revolutionized ML. Recurrent neural networks (RNNs) traditionally process one word at a time, significantly limiting scaling potential. Transformers introduced a self-attention mechanism where each word is connected to all other words, and attention learns how much to focus on each word. This significantly improved computation time because these operations could be parallelized and outperform capturing long-range spatial and temporal dependencies compared to RNNs. Since all the words are processed simultaneously, information on the position of word order is lost. Word positions are incorporated into input embeddings through PEs using sine and cosine functions to ensure each word has a unique representation. Then, they are projected to obtain queries (Q), keys (K), and values (V) with the hidden dimension size, and attention weights are computed using a scaled dot-product. Instead of learning single attention weights, they found it beneficial to learn multiple weight representations, as each attention could learn different representations of the same input, resulting in stable learning (Vaswani et al., 2017). Finally, the values from the attention layer are passed through a series of feedforward layers with residual connection after each layer to ensure smooth gradient flow. The transformer consists of encoder and decoder blocks; however, only the encoder block is used for our task, as discussed above.

Zhou et al. (2020) provided a detailed review of graph neural networks; interested readers could refer to that. A graph (G) consists of nodes (N) connected through edges (E) and denoted as G(N, E). Unlike text data, graphs contain edge details and are irregularly connected, implying that nodes exist in non-Euclidian space (Zhou et al., 2020). Thus, despite the transformer's success in natural language processing, it cannot be directly applied to the graph structure as it does not fully utilize the information in the graph structural topology and edges, and it is unclear what PEs mean when using sine and cosine. The GT architecture proposed by Dwivedi and Bresson (2020) comprises several aspects, such as the attention mechanism for a node being considered only between connected nodes and the Laplacian encoder instead of sine and cosine PE. They argued that Laplacian PEs (Eq. 10) generalize sine and cosine PEs for the graph structure.

$$\Delta = I - D^{-1/2} A D^{1/2} = U^T \Lambda U \quad (10)$$

In Eq. 10,  $A$  is the adjacency matrix,  $I$  is the identity matrix,  $D$  is the degree matrix,  $U$  and  $\Lambda$  are the eigenvectors and eigenvalues, respectively, from which  $k$  smallest non-trivial eigenvectors are obtained and used as PEs for a node (Dwivedi & Bresson, 2020). The obtained PEs are concatenated with the input node features projected to the hidden dimension ( $H$ ). Assuming multi-heads ( $n_{heads}$  number), the size of each head is thus  $d_k = H/n_{heads}$ . Scaled dot-product attention,  $A(Q, K)$ , for a single head,  $i$ , is computed using Eq. 11. The obtained attention scores are scaled by the edge weights ( $W_E$ ), given by Eq. 12 ( $\odot$  corresponds to element-wise multiplication), which are used to compute the attention output (Eq. 13), and concatenated from all the heads to obtain final layer output. Finally, the obtained multi-head output is passed through feedforward layers with residual connections followed by layer normalization after each layer (Zhang et al., 2024).

$$A(Q, K) = softmax\left(\frac{QK^T}{\sqrt{d_k}}\right) \quad (11)$$

$$A' = (I + A) \odot W \square_E \quad (12)$$

$$Z_i = A' V \quad (13)$$

## 4.2 Graph Construction

In this section, details of the graph construction are discussed. The graph nodes are locations of flooded and non-flooded points considered, with the final flooding factors as node features. A transformer connects all possible nodes, forming a complete graph (Vaswani et al., 2017). However, it is computationally expensive and scales poorly as the size of the graph increases. Hence, instead of connecting each node with all other nodes, it only connects with similar node features (Zhang et al., 2024; Belvederesi et al., 2025). Thus, with local connections, GT can scale better for large watersheds. The principal components of node features are then obtained, retaining 95% variance and cosine similarity between all the nodes, which is computed using the encoded principal component representation. Finally, each node is connected with itself, and the top  $k$  nodes (a hyperparameter) have the highest cosine similarity. It results in a directed graph. Edge weight could represent flow direction or proximity, but the cosine similarity value is used as edge weight in the present work. The flood susceptibility problem corresponds to a node-level prediction task – the probability of a node being flooded. The binary cross-entropy loss function is considered as it is a classification task.

## 4.3 Graph Transformer Results

The following are considered as hyperparameters: number of eigenvectors, number of neighbors each node is connected to, number of multi-heads, hidden layer dimension, number of transformer layers, dropout to prevent overfitting, learning rate, and the dimension of feedforward layer and optimized in Optuna. The obtained hyperparameters are shown in Table S2. Table 2 shows the GT model metrics. It can be observed that the GT model outperforms all models except XGBoost, with an AUC-ROC value of 0.9739, implying the model's superiority in discriminating flooded and non-flooded regions effectively and a specificity of 0.9426, implying that the model can accurately identify true positives. However, since the training data size is relatively small, decision tree methods perform slightly better than GT (Grinsztajn et al., 2022). Using datasets across multiple domains, Grinsztajn et al. (2022) demonstrated that decision tree models outperform deep learning approaches (e.g., GT) for training data of less than

10K samples. The GT model can leverage data effectively for large watersheds (e.g., national scale) and learn complex patterns better than traditional ML models. For instance, Lam et al. (2023) developed GraphCAST, a novel graph architecture-based global weather forecast, which outperforms deterministic simulations for 90% of the target variables.

The area of each class and the length of the railway track in each class are shown in Table 3. As illustrated in Fig. 6, the GT model has improved spatial coherence in high-susceptibility zones compared to fragmented predictions from RF/XGBoost with more precise boundary delineation. Interestingly, the GT and RF models have similar susceptibility patterns, especially along the channel networks and the upper Alps mountainous regions. Additionally, the percentage of areas in these two zones of these two models was similar, implying a consistent identification of flood-prone regions. However, the length of the track in high and very-high susceptibility classes (51.2%) is slightly lower than the RF model (63.29%) but closer to the ground-truth flooded track length (35%). The stark contrast between the GT and other models is its ability to sharply and coherently delineate the class boundaries compared to fragmented class boundaries in the RF model (especially evident for the low susceptibility in the Argens basin). The GT model slightly overpredicts moderate susceptibility in the mountainous regions and requires more computation (< 60 s for one Optuna run) and memory than the decision tree (< 10 s for one Optuna run) models. The GT model's superior spatial delineation could be attributed to the graph-based attention mechanism and Laplacian position encoders.

The permutation approach (Fisher et al., 2019) was used on the GT model to understand the importance of global features, as shown in Fig. 7. Input features were permuted 100 times across bootstrap iterations to ensure robustness to obtain 2.5 and 97.5 percentile, lower and upper bounds to obtain 95% confidence intervals. The importance values are normalized for better interpretation. The significance threshold is defined as the importance value if all the features are equal ( $=1/24$ ) and is also plotted. It can be observed that elevation, distance to channel, slope, and convergence index are the top four critical features, with values of 0.22, 0.13, 0.12, and 0.11, respectively. The tight confidence bounds for all the features imply statistical confidence in the obtained results. These features are consistently observed as important in RF and XGBoost models, indicating that these might be the most important features affecting flood susceptibility in this region, and all the models have learned meaningful features. Unlike XGBoost, the GT model does not strongly depend on a few features.

Additionally, lithology, NDBI, soil type, and lowest eigenvector are close to the threshold. The considered Laplacian PEs indeed provide meaningful information; however, as we should expect, node features dominate and not the graph structure in importance. Interestingly, precipitation and LULC have a minor and negligible influence, respectively, on flood susceptibility. While current precipitation/LULC shows limited influence, their projected future values may amplify importance in scenario-based analyses.

Furthermore, we explore whether the Laplacian PEs can exploit the graph structure and provide meaningful information to the node features. In this regard, t-distributed stochastic neighbor embedding (t-SNE) (Van der Maaten & Hinton, 2008) and Uniform Manifold Approximation and Projection (UMAP) (McInnes et al., 2020) techniques are used to understand PE embeddings, as shown in Fig. 8 with blue color for non-flooded and red for flooded. t-SNE is a nonlinear technique that preserves local structure - points close in the higher dimension will be close in the projected low-dimensional space (Van der Maaten & Hinton, 2008). In contrast, UMAP balances to preserve local and

global structures. The non-flooded and flooded nodes are separated, especially in the bottom left and right, respectively, of the t-SNE plot. Similarly, UMAP revealed partial clustering, especially the non-flooded nodes in the left part and flooded nodes in the bottom part of the plots. However, they are not separated in many regions, indicating that PEs could not fully distinguish between the flooded and non-flooded regions. A similar conclusion was drawn from Fig. 7, where flooding factors had higher importance than positional encodings.

The Moran's I scatterplot for the GT model is shown in Fig. 9 with Moran's I value = 0.6119 (p-value < 0.0001) and Z-score = 161.5528. Since these values are higher than the RF and XGBoost models, the GT model could capture spatial autocorrelations better. Using Laplacian PEs and graph structure with an attention mechanism enhanced the spatial information of the model. Finally, the Monte Carlo (MC) dropout technique was applied during inference by enabling dropout during testing, and the GT model predictions are considered for 100 stochastic forward passes to estimate epistemic uncertainty. The computed standard deviations (i.e., uncertainty) shown in Fig. S7 (supplementary) are predominantly below 0.03. Interestingly, predictions for the very-low and many very-high susceptibility classes exhibit the lowest uncertainty (< 0.01), suggesting robust detection of critical regions prone to flooding. The following section uses the GT model to generate flood susceptibility maps for future scenarios.

## 5. Flood Susceptibility for Future Scenarios

Nguyen et al. (2024) observed a rapid increase in flood risk from 2005 to 2020 and predicted it would further increase in 2035 and 2050. They point to this increase due to changes in LULC and precipitation. Hence, this section understands the impact of future precipitation and LULC changes on the flood susceptibility maps for the French Riviera. In this regard, the projected precipitation values are obtained for RCP 2.6, RCP 4.5, and RCP 8.5 from the Drias portal<sup>4</sup>, which is a joint research collaboration between Météo-France, IPSL, CERFACS, CNRM (Météo-France et al., 2025). They provide projections using several models, and in the present work, data from the regional climate ALADIN63\_CNRM-CM5 model from the Drias 2020 dataset are obtained for the 2050 year. Annual precipitation values range from 835 mm to 1366 mm, 781 mm to 1460 mm, and 806 mm to 1485 mm for the watershed under RCP 2.6, RCP 4.5, and RCP 8.5, respectively, compared to a maximum mean annual value of 943 mm under current conditions. Additionally, projected LULC values for the 2050 year are obtained from the ArcGIS web map: Living Atlas of the World with 300 m resolution (Clark University, 2021). They obtained projected LULC values for the year 2050 using ESA land cover values from 2010 to 2018. A significant change was observed in crop areas, which increased from 1.23% to 23.46%, and the remaining classification areas slightly decreased.

We assume all the remaining flooding factors except projected annual precipitation and LULC values obtained for 2050 are unchanged. Fig. 10, Fig. S8, and Fig. S9 (supplementary) show the flood susceptibility plots for the RCP 2.6, RCP 4.5, and RCP 8.5 scenarios, respectively. It can be observed that significantly larger regions are classified as high and very-high susceptible, agreeing well with other works (Janizadeh et al., 2021; Nguyen et al., 2024), with a noticeable change observed in the Siagne catchment. Table 4 shows the area of each class and the length of railway tracks in each class for the year 2050. A considerable section of the area is classified as very-high susceptibility: 16.57%, 13.75%, and 17.46% under RCP 2.6, RCP 4.5, and RCP 8.5 scenarios, respectively, up from 6.19% under current

---

<sup>4</sup> <https://www.drias-climat.fr/> (last accessed on 15 October 2024)

conditions. Similar changes were evident across all classes (except very low), with an increased percentage of areas. Additionally, the channel downstream sections were classified as very-large susceptibility; consequently, a significant portion of the track length is under this class in all the forecasted scenarios, with values above 52%, up from 35.61% under current conditions. Furthermore, RCP 8.5 is the worst-case scenario, and we observe a slightly higher area corresponding to the very-high susceptibility class than other scenarios. Surprisingly, the RCP 4.5 scenario has a lower very-high susceptible area than the RCP 2.6 scenario, and a similar trend was observed by Janizadeh et al. (2021), where the area of very-high susceptibility was higher for the RCP 2.6 scenario than the RCP 8.5 scenario.

Finally, we assess the factors affecting this significant increase in flood susceptibility, as shown in Fig. S10 (supplementary), which is plotted for the future estimated data. It can be observed that the importance of elevation, slope, convergence index, and distance to the channel decreased using the forecasted data. Since annual precipitation values increased, its importance significantly increased. Similarly, increased precipitation directly affects the drainage density and lithology, resulting in their importance. The importance of NDBI could have also increased flood susceptibility in urban areas corresponding to the Siagne catchment. Interestingly, LULC has a limited effect on the model's performance; perhaps the 300 m coarse resolution was insufficient. Finally, the importance of PEs significantly increases, implying that the spatial relationships are more critical for future scenarios.

## 6. Conclusions

The present research addresses a critical gap in flood risk management for the French Riviera – a region experiencing multiple disastrous floods in the past decades. Our work introduces the first graph transformer-based flood susceptibility analysis that outperforms traditional ML approaches and provides a quantitative railway vulnerability for the current and future scenarios.

In this regard, we initially performed flood susceptibility analysis using ML approaches frequently used in the literature. Flooding factors corresponding to topography, hydrology, geology, and environment are considered. The performance of models was assessed using binary metrics such as AUC-ROC, sensitivity, specificity, PPV, and NPV. XGBoost model had the highest values in all the metrics, followed by random forest. ANN significantly underperformed, perhaps due to a smaller dataset size where decision tree methods outperform other architectures, as also noted by others (e.g., Grinsztajn et al., 2022). However, when susceptibility maps were qualitatively verified, the RF model identified classification boundaries more effectively than the XGBoost model. SHAP plots provided insight into why this could happen: XGBoost's overreliance on a few parameters was not the case with the RF model. However, both models suggested elevation, slope, distance to channel, and convergence index as the influencing parameters, indicating that the models could learn actual flood processes. Spatial autocorrelations further validated the above conclusion: XGBoost had a Moran's I value of 0.5311 ( $p < 0.0001$ ), whereas RF had 0.5775 ( $p < 0.0001$ ), indicating that the RF model learned better spatial autocorrelations, resulting in better transitions from one susceptible class to another. Since flood classification is a multi-classification problem, we concluded that binary metrics cannot fully explain the model's performance. Despite the RF model's superiority over XGBoost, it fails to identify sharp boundaries precisely.

We proposed that GT learns spatial features better than traditional ML approaches as they are incorporated into the node features. We used Laplacian PEs and demonstrated that they could identify flooded and non-flooded decision boundaries using t-SNE and UMAP techniques. However, PEs' influence on model prediction was limited as flooding factors dominated the model prediction. Interestingly, the flooding factors influencing RF and XGBoost models were the top four factors for the GT model. The GT model had slightly lower metrics than XGBoost but higher metrics than others.

Additionally, when the flood susceptibility map was qualitatively assessed, sharp and abrupt class boundaries were evident in this plot. The Moran's I value for GT was 0.6119 ( $p < 0.0001$ ), significantly higher than the XGBoost and RF models, indicating that the GT model could effectively delineate the class boundaries. Our GT framework serves as a replicable blueprint that others could replicate in other regions with potential regional adaptation needs. XGBoost underestimated high-susceptibility zones, and approximately 15% of the area corresponded to high and very-high susceptibility classes for both the RF and GT models. The flooding effect on the railway infrastructure was assessed by computing the length of tracks susceptible to flooding, and the GT model predicted that 35.61% of the length corresponded to the very-high susceptible class.

Finally, the effect of climate and LULC change on the flood susceptibility prediction was assessed for the 2050 year using the GT model under RCP 2.6, RCP 4.5, and RCP 8.5 scenarios. Except for the very-low susceptibility class, areas of all other classes increased compared to current conditions, with 17.46% of the area estimated as very-high under the RCP 8.5 scenario, and 54% of track length corresponded to it. A pronounced effect was observed in the Siagne catchment. The importance of precipitation, NDBI, and drainage density increased using forecasted data. Interestingly, LULC had limited importance (possibly due to 300 m coarser resolution), and PEs had increased importance, indicating spatial relations are important for future projections.

The outcome of our work can inform authorities in infrastructure planning and mitigation strategies. For instance, the AI predictive tool developed in this paper may steer the construction of flood barriers to protect railway lines, elevate tracks to minimize the risk of water logging, and use corrosion-resistant materials to minimize water-induced damage.

The major limitation of the present work on railway tracks is that the obtained flooding probability does not directly translate into track flooding since track elevation is ignored. Training a GT model is computationally challenging compared to traditional ML models. However, for a given region, the graph architecture could be precomputed, and inference time is significantly reduced, potentially enabling its integration with hydraulic models and use for real-time flood management. The model predictions could be further enhanced by incorporating precipitation, LULC, NDBI, and other factors varying temporally to obtain future flood susceptibility. Different positional encoders, node embeddings, node and edge features, and graph architectures could be explored. The developed flood susceptibility must be incorporated into the multi-hazard framework for a holistic estimate of regional hazards.

## **Data Availability**

All the data used to support our results are publicly available.

## **Author Contribution**

Vemula Sreenath: conceptualization, methodology, software, validation, formal analysis, investigation, data curation, writing – original draft, visualization. Filippo Gatti: conceptualization, methodology, resources, writing – review & editing, project administration. Pierre Jehel: conceptualization, resources, writing – review & editing, project administration, funding acquisition.

## **Declaration of generative AI in scientific writing**

While preparing the manuscript, the authors used generative AI tools such as ChatGPT, Claude, and Perplexity to improve the readability and correct the language. After using these tools, the author(s) reviewed and edited the content as required and take(s) full responsibility for the content of the published article.

## **Acknowledgments**

The authors acknowledge and appreciate the contributions of several organizations for their efforts and for making data publicly available: Météo-France for current precipitation values, SNCF for railway tracks, géographiques IDE for inundation maps, and IGN for DEM. The DRIAS climate services portal provided the climate projections data used in this study, which Météo-France and the national climate scientific community (IPSL, CERFACS, CNRM) implemented. Clark University developed the forecasted LULC data used in this study in partnership with Esri.

## **Funding**

This research was carried out in the Minerve project. The Minerve project is supported by the French government within the France 2030 framework. The authors thankfully acknowledge this support.

## **Declaration of competing interest**

The authors declare that no competing financial interests or personal relationships could have influenced this work.

Table 1. Variance inflation factor (VIF) and Tolerance (TOL) for the final flooding inputs

S. No.	Feature	VIF	TOL
0	Elevation	4.099	0.244
1	Slope	6.180	0.162
2	Aspect	4.634	0.216
3	Plan Curvature	1.092	0.916
4	Convergence Index	1.722	0.581
5	Topographic Position Index	1.634	0.612
6	Slope Length Factor	3.877	0.258
7	Drainage Density	7.687	0.130
8	Stream Power Index	2.341	0.427
9	Distance to Road	1.990	0.502
10	Distance to Channel	3.610	0.277
11	Mean Annual Precipitation	32.422	0.031
12	LULC	4.313	0.232
13	Soil Type	10.131	0.099
14	NDBI max	1.459	0.685
15	Lithology	2.408	0.415

Table 2. Performance metrics of the ML and GT models for the testing dataset.

Model	AUC-ROC	Sensitivity	Specificity	PPV	NPV
ANN	0.915	0.8333	0.8138	0.8453	0.8205
SVC	0.9527	0.9	0.884	0.8858	0.8984
RF	0.9786	0.932	0.92	0.9209	0.9312
XGBoost	0.9853	0.944	0.94	0.9402	0.9438
GT	0.9739	0.9426	0.9264	0.9274	0.9417

Table 3. The area of each susceptibility class and the track length in each class.

Model	Very Low	Low	Moderate	High	Very High
ANN (Area)	29.30%	29.44%	23.07%	13.83%	4.36%
ANN (Length)	1.00%	8.95%	17.20%	39.88%	32.97%
SVC (Area)	28.15%	39.55%	19.52%	9.94%	2.85%
SVC (Length)	3.64%	26.35%	18.67%	26.73%	24.61%
RF (Area)	37.85%	29.44%	17.40%	9.20%	6.11%
RF (Length)	2.14%	18.53%	16.04%	23.44%	39.85%
XGBoost (Area)	0.78%	67.15%	22.31%	7.73%	2.03%
XGBoost (Length)	0.41%	14.92%	30.62%	37.91%	16.14%
GT (Area)	52.95%	19.30%	12.48%	9.07%	6.19%
GT (Length)	22.87%	14.37%	11.56%	15.59%	35.61%

Table 4. Area of each susceptibility class and the track length in each class for 2050.

Variable	Very-low	Low	Moderate	High	Very-high
RCP 2.6 (Area)	26.13%	21.37%	18.71%	17.22%	16.57%
RCP 2.6 (Length)	5.66%	14.98%	11.85%	11.96%	55.55%
RCP 4.5 (Area)	28.64%	22.89%	18.75%	15.97%	13.75%
RCP 4.5 (Length)	8.87%	16.33%	12.12%	10.25%	52.43%
RCP 8.5 (Area)	25.82%	21.49%	18.29%	16.94%	17.46%
RCP 8.5 (Length)	9.44%	12.87%	13.29%	10.40%	54.00%

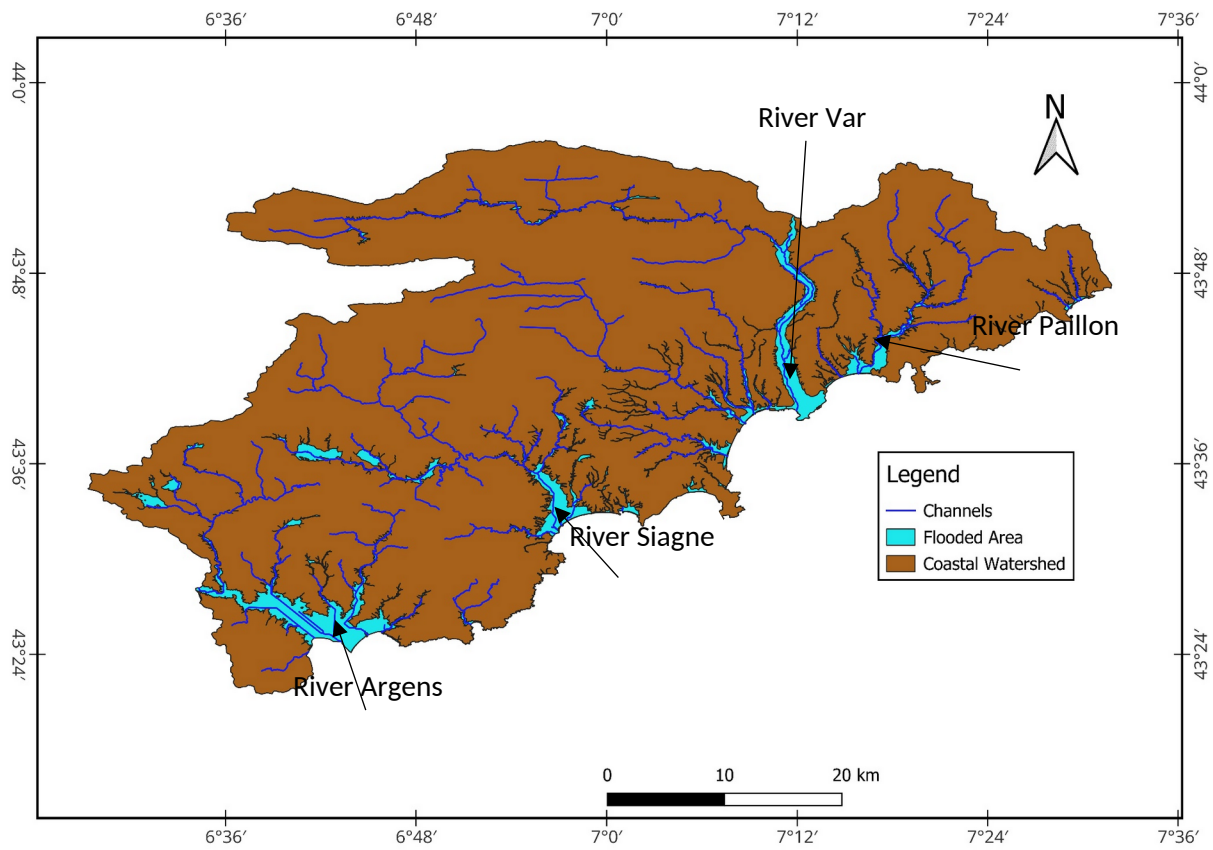


Figure 1 Inundation map of the French Riviera along with channels derived from DEM.

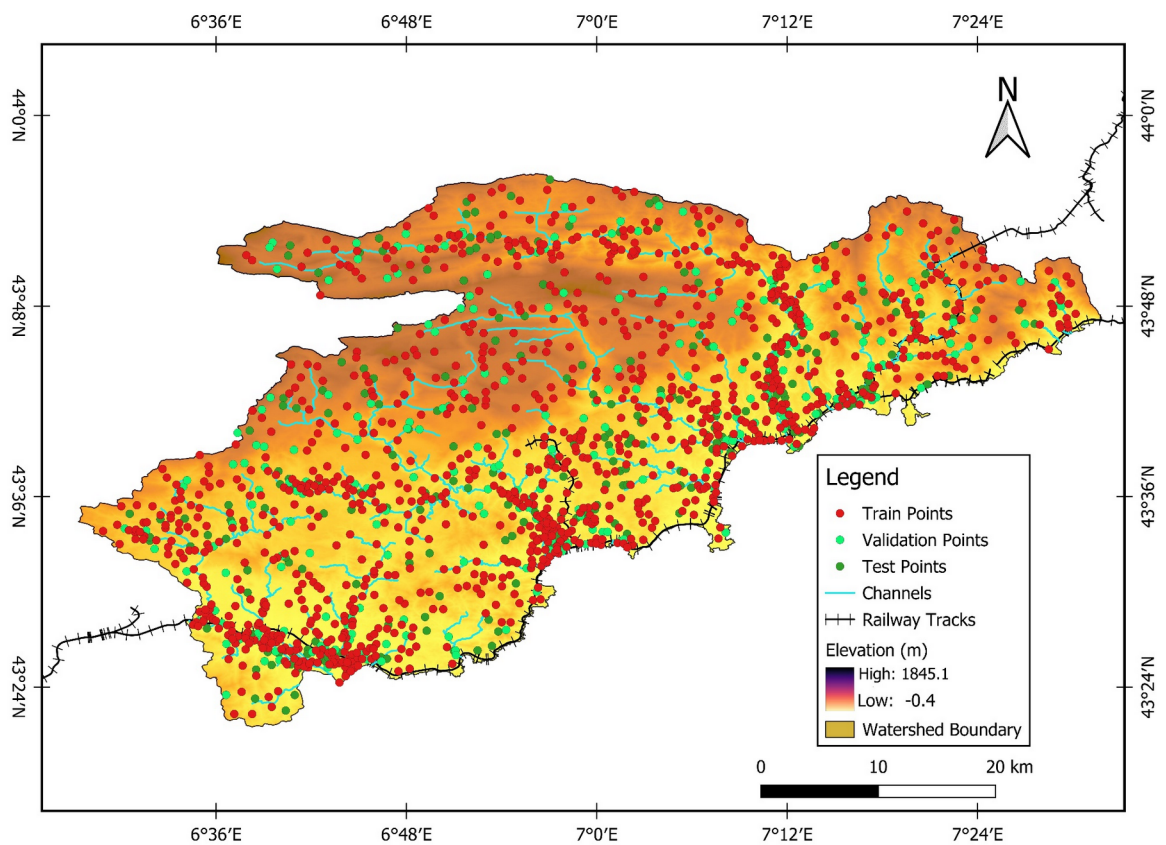


Figure 2 Plot showing training, validation, and testing points for the GT model and railway track.

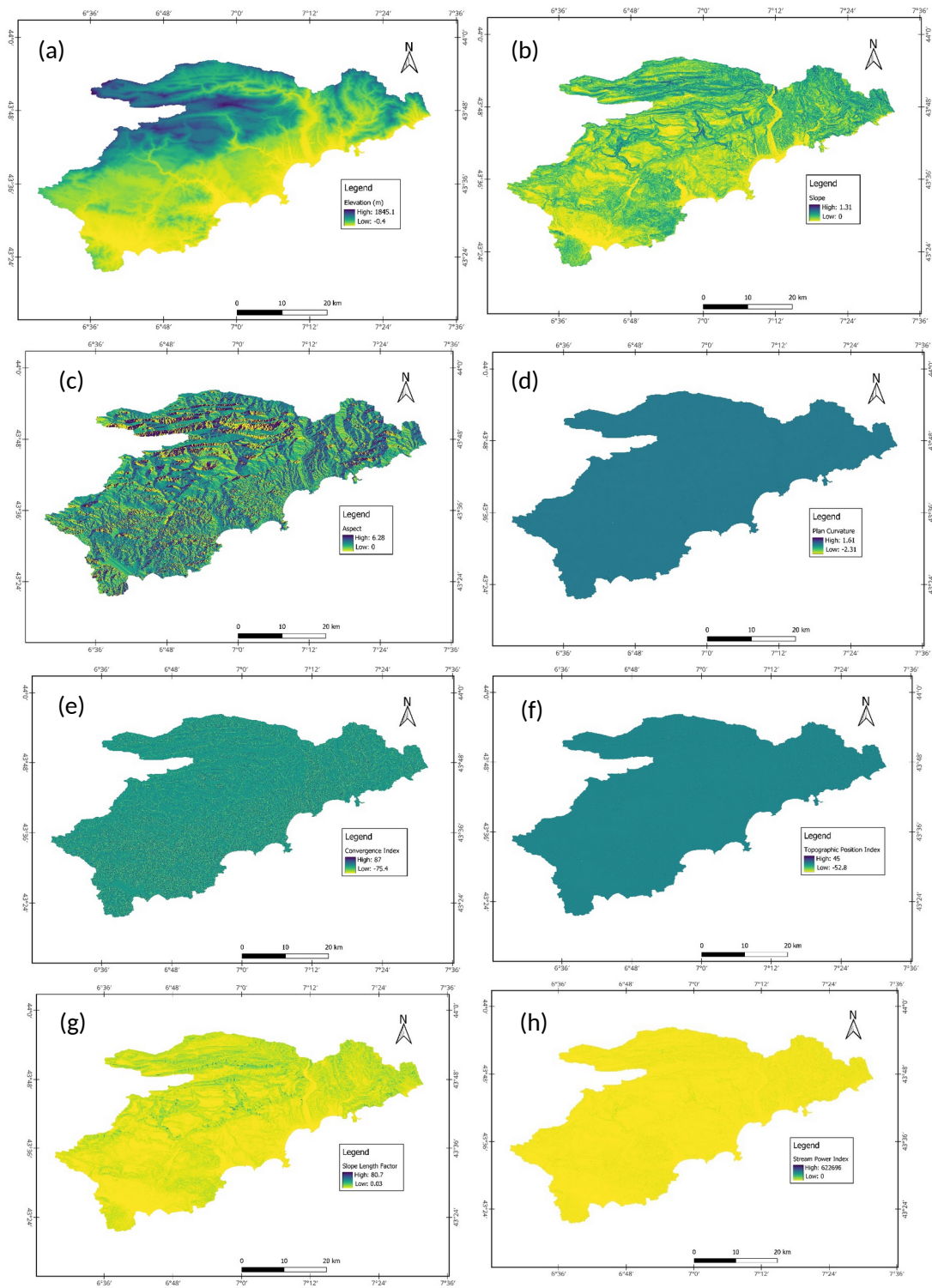


Figure 3. Flood influencing factors: (a) elevation, (b) slope, (c) aspect, (d) plan curvature, (e) convergence index, (f) topographic position index, (g) slope length factor, (h) stream power index.

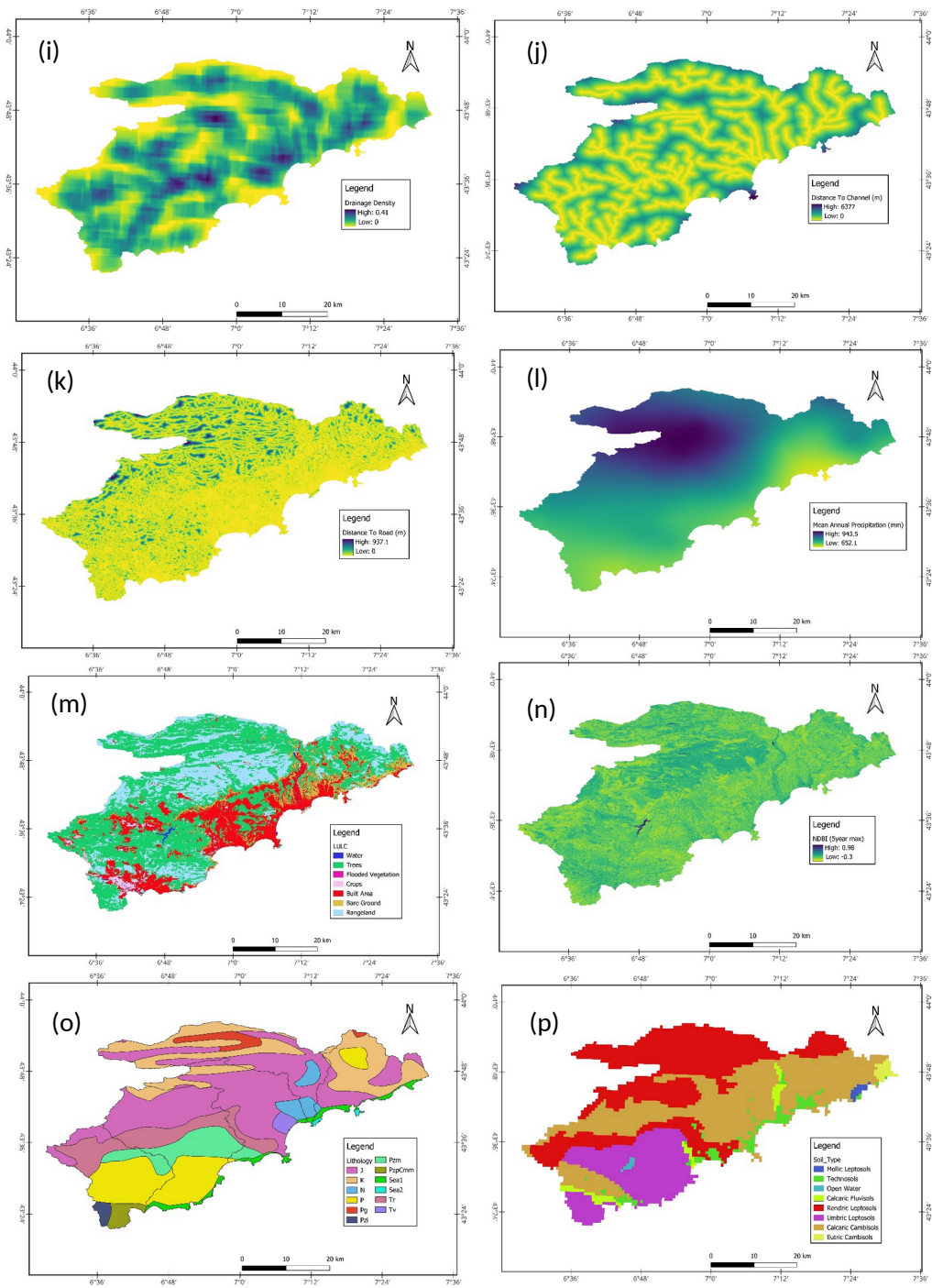


Figure 3. Flood influencing factors (contd.): (i) drainage density, (j) distance to channel, (k) distance to road, (l) mean annual precipitation, (m) LULC, (n) NDBI, (o) lithology, and (p) soil type.

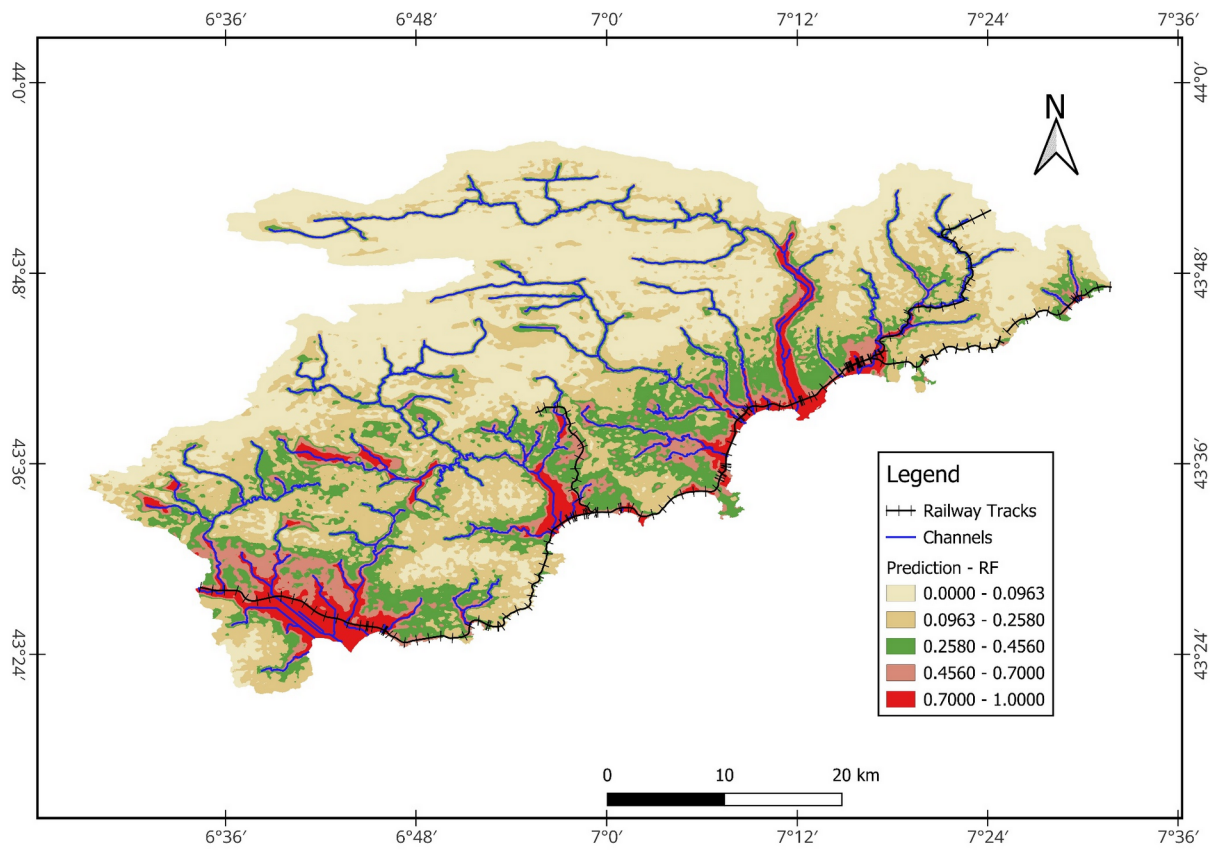


Figure 4. Flood susceptibility plot using the RF model.

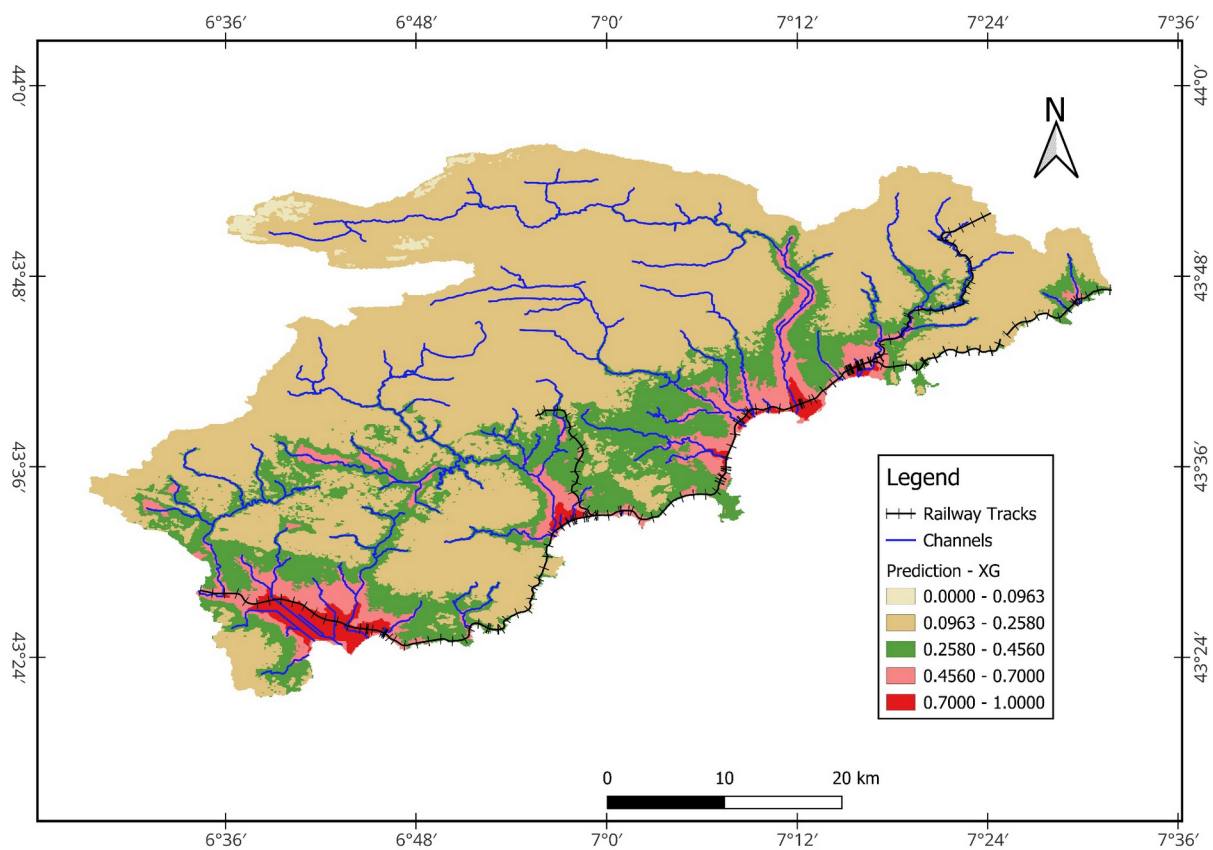


Figure 5. Flood susceptibility plot using the XGBoost model.

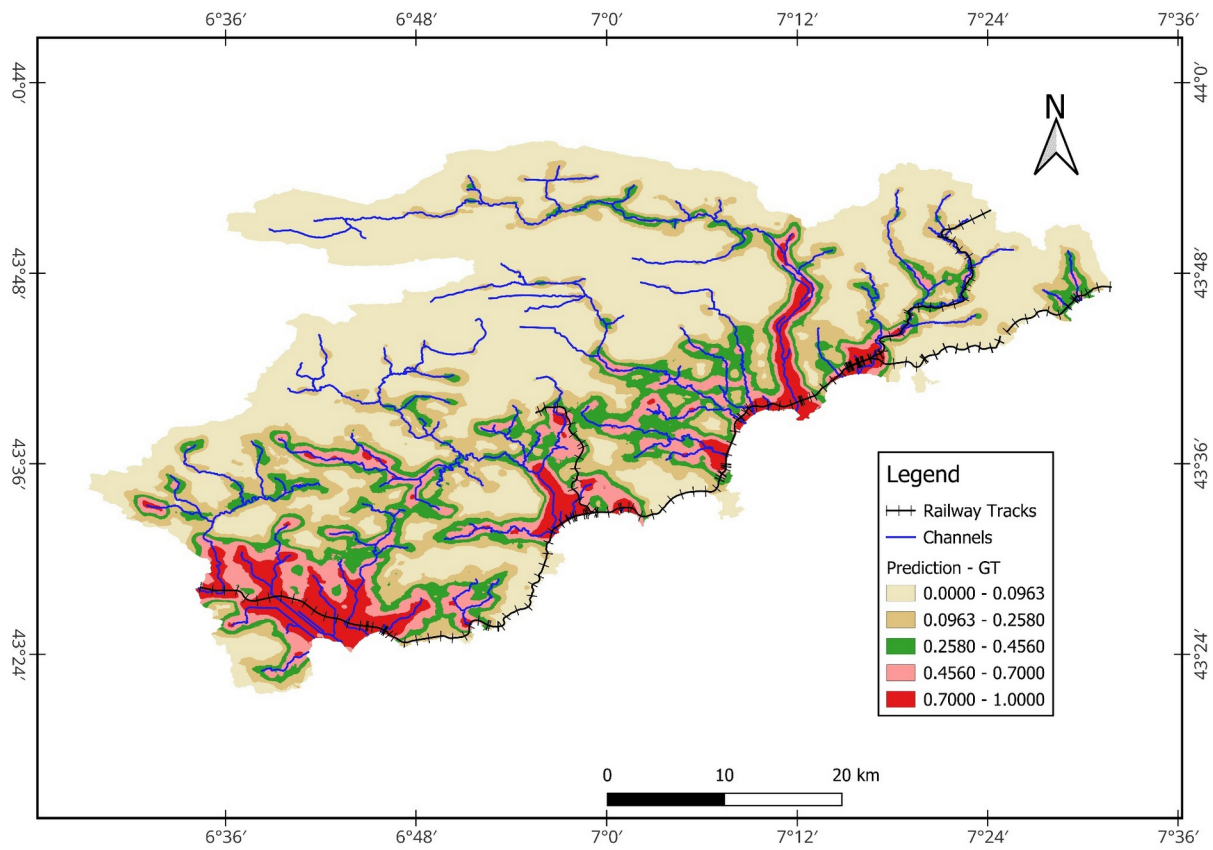


Figure 6. Flood susceptibility plot using the GT model.

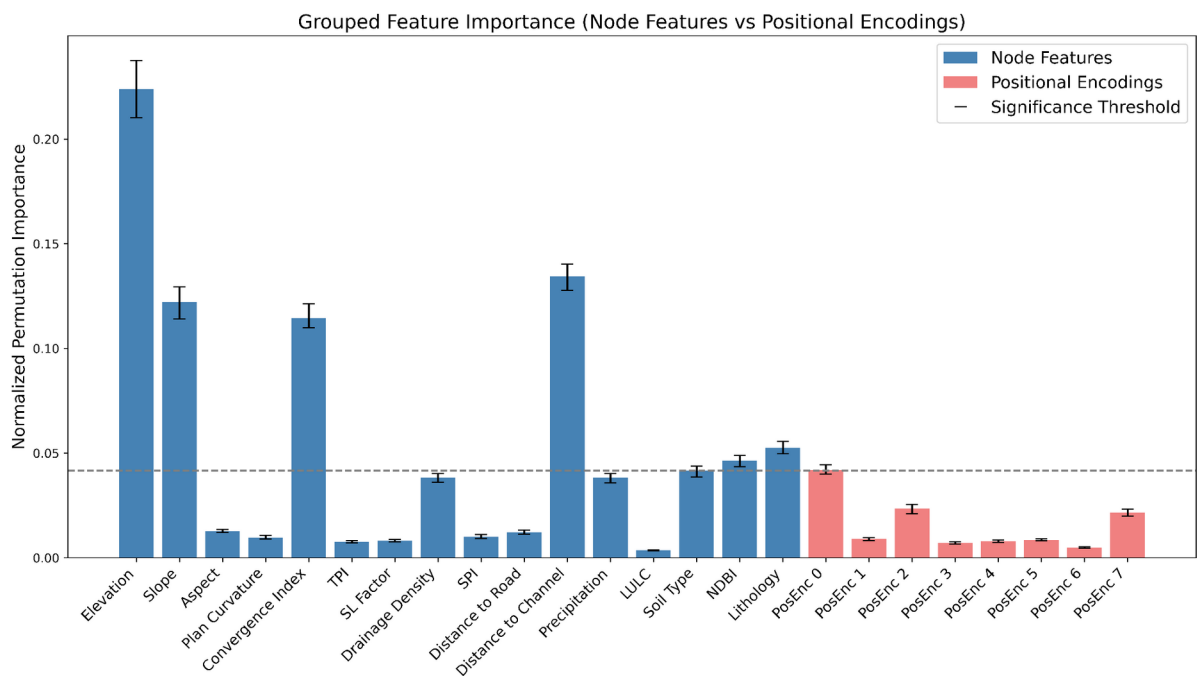


Figure 7. Global feature importance using the permutation method.

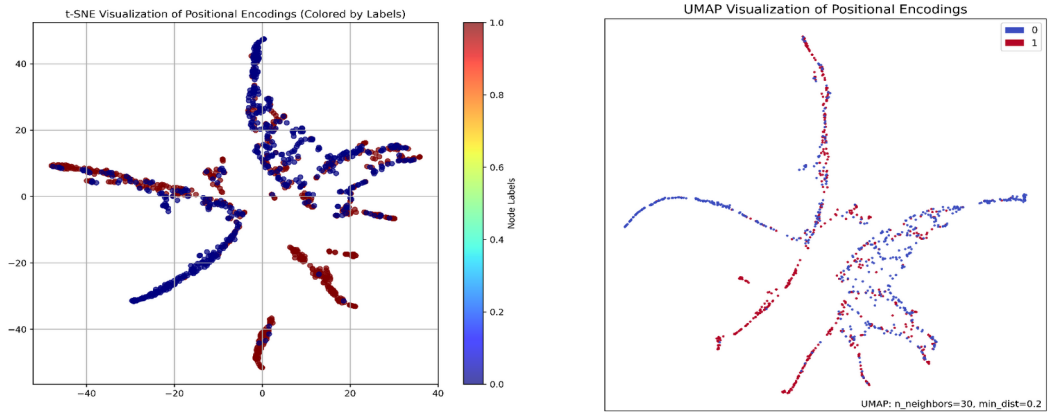


Figure 8. The t-SNE (left) and UMAP (right) visualizations of the GT model positional encodings.

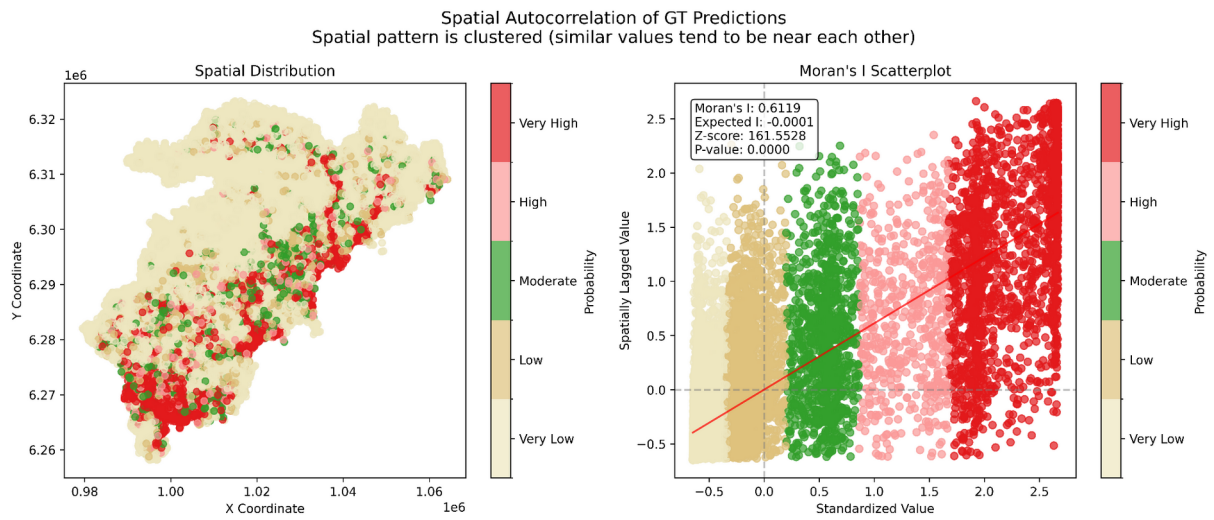


Figure 9. Moran's I Spatial Autocorrelation plot for the GT Model.

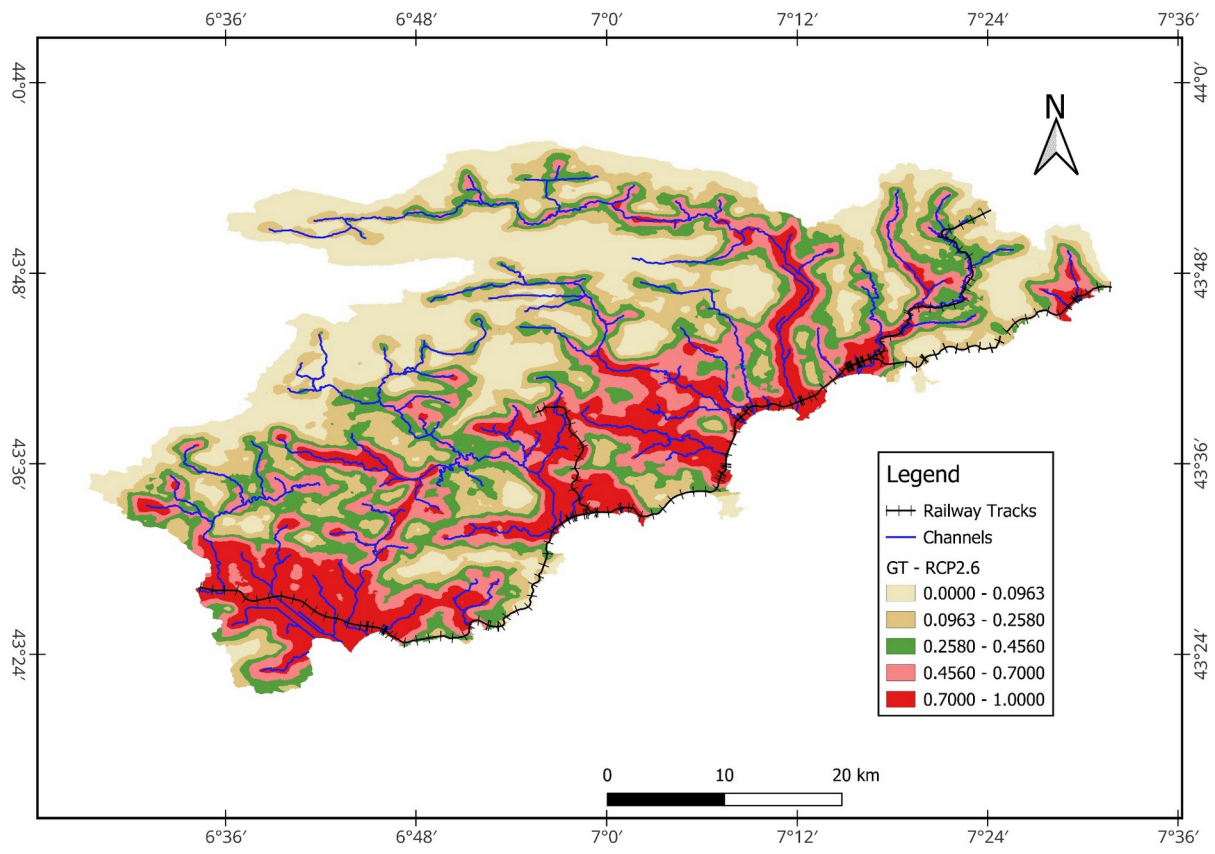


Figure 10. Projected flood susceptibility plot using the GT model for the year 2050, RCP 2.6 scenario.

## References

- Abedi, R., Costache, R., Shafizadeh-Moghadam, H., & Pham, Q. B. (2022). Flash-flood susceptibility mapping based on XGBoost, random forest and boosted regression trees. *Geocarto International*, 37(19), 5479-5496. DOI: 10.1080/10106049.2021.1920636.
- Addis, A. (2023). GIS-based flood susceptibility mapping using frequency ratio and information value models in the upper Abay river basin, Ethiopia. *Natural Hazards Research*, 3(2), 247-256. DOI: 10.1016/j.nhres.2023.02.003.
- Ahmadlou, M., Al-Fugara, A. K., Al-Shabeeb, A. R., Arora, A., Al-Adamat, R., Pham, Q. B., ... & Sajedi, H. (2021). Flood susceptibility mapping and assessment using a novel deep learning model combining multilayer perceptron and autoencoder neural networks. *Journal of Flood Risk Management*, 14(1), e12683. DOI: 10.1111/jfr3.12683.
- Ahmed, N., Hoque, M. A. A., Arabameri, A., Pal, S. C., Chakraborty, R., & Jui, J. (2022). Flood susceptibility mapping in Brahmaputra floodplain of Bangladesh using deep boost, deep learning neural network, and artificial neural network. *Geocarto International*, 37(25), 8770-8791. DOI: 10.1080/10106049.2021.2005698.
- Akay, H. (2021). Flood hazards susceptibility mapping using statistical, fuzzy logic, and MCDM methods. *Soft Computing*, 25(14), 9325-9346. DOI: 10.1007/s00500-021-05903-1.
- Akiba, T., Sano, S., Yanase, T., Ohta, T., & Koyama, M. (2019, July). Optuna: A next-generation hyperparameter optimization framework. In *Proceedings of the 25th ACM SIGKDD international conference on knowledge discovery & data mining* (pp. 2623-2631). DOI: 10.48550/arXiv.1907.10902.
- Arabameri, A., Seyed Danesh, A., Santosh, M., Cerda, A., Chandra Pal, S., Ghorbanzadeh, O., ... & Chowdhuri, I. (2022). Flood susceptibility mapping using meta-heuristic algorithms. *Geomatics, Natural Hazards and Risk*, 13(1), 949-974. DOI: 10.1080/19475705.2022.2060138.
- Belvederesi, G., Tanyas, H., Lipani, A., Dahal, A., & Lombardo, L. (2025). Distribution-agnostic landslide hazard modelling via Graph Transformers. *Environmental Modelling & Software*, 183, 106231. DOI: 10.1016/j.envsoft.2024.106231.
- Bentivoglio, R., Isufi, E., Jonkman, S. N., & Taormina, R. (2022). Deep learning methods for flood mapping: a review of existing applications and future research directions. *Hydrology and Earth System Sciences Discussions*, 2022, 1-50. DOI: 10.5194/hess-26-4345-2022, 2022.
- Breiman, L. (2001). Random forests. *Machine learning*, 45, 5-32. DOI: 10.1023/A:1010933404324.
- Bubeck, P., Dillenardt, L., Alfieri, L., Feyen, L., Thieken, A. H., & Kellermann, P. (2019). Global warming to increase flood risk on European railways. *Climatic Change*, 155, 19-36. DOI: 10.1007/s10584-019-02434-5.
- Bui, D. T., Tsangaratos, P., Ngo, P. T. T., Pham, T. D., & Pham, B. T. (2019). Flash flood susceptibility modeling using an optimized fuzzy rule based feature selection technique and tree based ensemble methods. *Science of the total environment*, 668, 1038-1054. DOI: 10.1016/j.scitotenv.2019.02.422.
- Bui, Q. T., Nguyen, Q. H., Nguyen, X. L., Pham, V. D., Nguyen, H. D., & Pham, V. M. (2020). Verification of novel integrations of swarm intelligence algorithms into deep learning neural network for flood susceptibility mapping. *Journal of Hydrology*, 581, 124379. DOI: 10.1016/j.jhydrol.2019.124379.
- Chapi, K., Singh, V. P., Shirzadi, A., Shahabi, H., Bui, D. T., Pham, B. T., & Khosravi, K. (2017). A novel hybrid artificial intelligence approach for flood susceptibility assessment. *Environmental Modelling & Software*, 95, 229-245. DOI: 10.1016/j.envsoft.2017.06.012.
- Cheetham, M., Chirouze, F., & Bredier, L. (2016). RISK VIP: Evaluation of Flood Risk on the French Railway Network Using an Innovative GIS Approach. In *E3S Web of Conferences* (Vol. 7, p. 10004). EDP Sciences. DOI: 10.1051/e3sconf/20160710004.
- Chen, T., & Guestrin, C. (2016, August). Xgboost: A scalable tree boosting system. In *Proceedings of the 22nd ACM SIGKDD International Conference on Knowledge Discovery and Data Mining* (pp. 785-794). DOI: 10.1145/2939672.2939785.

Chen, W., Li, Y., Xue, W., Shahabi, H., Li, S., Hong, H., ... & Ahmad, B. B. (2020). Modeling flood susceptibility using data-driven approaches of naïve Bayes tree, alternating decision tree, and random forest methods. *Science of The Total Environment*, 701, 134979. DOI: 10.1016/j.scitotenv.2019.134979.

Choubin, B., Moradi, E., Golshan, M., Adamowski, J., Sajedi-Hosseini, F., & Mosavi, A. (2019). An ensemble prediction of flood susceptibility using multivariate discriminant analysis, classification and regression trees, and support vector machines. *Science of the Total Environment*, 651, 2087-2096. DOI: 10.1016/j.scitotenv.2018.10.064.

Clark University. "Projected land cover in 2050" [Web Map]. Scale 1:50,000 and smaller. "ArcGIS Living Atlas of the World". April 2021. <https://www.arcgis.com/home/item.html?id=3cce97cba8394287bcaf60f7618a5500> - (20 February 2025)

Cortes, C., & Vapnik, V. (1995). Support-vector networks. *Machine learning*, 20, 273-297. DOI: 10.1007/BF00994018.

Conda-Forge Community. (2024). XGBoost: Scalable and Portable Gradient Boosting Library (Version 1.7.3) [Software]. Retrieved September 30, 2024, from <https://anaconda.org/conda-forge/xgboost>

Das, S. (2020). Flood susceptibility mapping of the Western Ghat coastal belt using multi-source geospatial data and analytical hierarchy process (AHP). *Remote Sensing Applications: Society and Environment*, 20, 100379. DOI: 10.1016/j.rsase.2020.100379.

Dwivedi, V. P., & Bresson, X. (2020). A generalization of transformer networks to graphs. arXiv preprint arXiv:2012.09699.

FAO & IASA. 2023. Harmonized World Soil Database Version 2.0. Rome and Laxenburg. DOI: 10.4060/cc3823en.

Fenglin, W., Ahmad, I., Zelenakova, M., Fenta, A., Dar, M. A., Teka, A. H., ... & Shafi, S. N. (2023). Exploratory regression modeling for flood susceptibility mapping in the GIS environment. *Scientific Reports*, 13(1), 247. DOI: 10.1038/s41598-023-27447-0.

Fisher, A., Rudin, C., & Dominici, F. (2019). All models are wrong, but many are useful: Learning a variable's importance by studying an entire class of prediction models simultaneously. *Journal of Machine Learning Research*, 20(177), 1-81. DOI: 10.48550/arXiv.1801.01489.

Gao, W., Liao, Y., Chen, Y., Lai, C., He, S., & Wang, Z. (2024). Enhancing transparency in data-driven urban pluvial flood prediction using an explainable CNN model. *Journal of Hydrology*, 645, 132228. DOI: 10.1016/j.jhydrol.2024.132228.

Gharbi, M., Soualmia, A., Dartus, D., & Masbernat, L. (2016). Comparison of 1D and 2D hydraulic models for floods simulation on the Medjerda River in Tunisia. *J. Mater. Environ. Sci*, 7(8), 3017-3026.

Ghosh, S., Saha, S., & Bera, B. (2022). Flood susceptibility zonation using advanced ensemble machine learning models within Himalayan foreland basin. *Natural Hazards Research*, 2(4), 363-374. DOI: 10.1016/j.nhres.2022.06.003.

Gilmer, J., Schoenholz, S. S., Riley, P. F., Vinyals, O., & Dahl, G. E. (2017, July). Neural message passing for quantum chemistry. In *International conference on machine learning* (pp. 1263-1272). PMLR. DOI: 10.48550/arXiv.1704.01212.

Ginesta, M., Yiou, P., Messori, G., & Faranda, D. (2023). A methodology for attributing severe extratropical cyclones to climate change based on reanalysis data: the case study of storm Alex 2020. *Climate Dynamics*, 61(1), 229-253. DOI: 10.1007/s00382-022-06565-x.

Grinsztajn, L., Oyallon, E., & Varoquaux, G. (2022). Why do tree-based models still outperform deep learning on typical tabular data? *Advances in neural information processing systems*, 35, 507-520.

Habibi, A., Delavar, M. R., Nazari, B., Pirasteh, S., & Sadeghian, M. S. (2023). A novel approach for flood hazard assessment using hybridized ensemble models and feature selection algorithms. *International Journal of Applied Earth Observation and Geoinformation*, 122, 103443. DOI: 10.1016/j.jag.2023.103443.

- Hong, H., Tsangaratos, P., Ilija, I., Liu, J., Zhu, A. X., & Chen, W. (2018). Application of fuzzy weight of evidence and data mining techniques in construction of flood susceptibility map of Poyang County, China. *Science of the total environment*, 625, 575-588. DOI: 10.1016/j.scitotenv.2017.12.256.
- Islam, A. R. M. T., Talukdar, S., Mahato, S., Kundu, S., Eibek, K. U., Pham, Q. B., ... & Linh, N. T. T. (2021). Flood susceptibility modelling using advanced ensemble machine learning models. *Geoscience Frontiers*, 12(3), DOI: 10.1016/j.gsf.2020.09.006.
- Jahanbani, M., Vahidnia, M. H., Aghamohammadi, H., & Azizi, Z. (2024). Flood susceptibility mapping through geoinformatics and ensemble learning methods, with an emphasis on the AdaBoost-Decision Tree algorithm, in Mazandaran, Iran. *Earth Science Informatics*, 17(2), 1433-1457. DOI: 10.1007/s12145-023-01213-2.
- Janizadeh, S., Pal, S. C., Saha, A., Chowdhuri, I., Ahmadi, K., Mirzaei, S., ... & Tiefenbacher, J. P. (2021). Mapping the spatial and temporal variability of flood hazard affected by climate and land-use changes in the future. *Journal of Environmental Management*, 298, 113551. DOI: 10.1016/j.jenvman.2021.113551.
- Karra, K., Kontgis, C., Statman-Weil, Z., Mazzariello, J. C., Mathis, M., & Brumby, S. P. (2021, July). Global land use/land cover with Sentinel 2 and deep learning. In *2021 IEEE International Geoscience and Remote Sensing Symposium IGARSS* (pp. 4704-4707). IEEE. DOI:10.1109/IGARSS47720.2021.9553499.
- Khalifeh Soltanian, F., Abbasi, M., & Riyahi Bakhtyari, H. R. (2019). Flood monitoring using NDWI and MNDWI spectral indices: A case study of Aghqala flood-2019, Golestan Province, Iran. *The international archives of the photogrammetry, remote sensing and spatial information sciences*, 42, 605-607. DOI: 10.5194/isprs-archives-XLII-4-W18-605-2019.
- Khosravi, K., Shahabi, H., Pham, B. T., Adamowski, J., Shirzadi, A., Pradhan, B., ... & Prakash, I. (2019). A comparative assessment of flood susceptibility modeling using multi-criteria decision-making analysis and machine learning methods. *Journal of Hydrology*, 573, 311-323. DOI: 10.1016/j.jhydrol.2019.03.073.
- Koks, E. E., Rozenberg, J., Zorn, C., Tariverdi, M., Vousdoukas, M., Fraser, S. A., ... & Hallegatte, S. (2019). A global multi-hazard risk analysis of road and railway infrastructure assets. *Nature communications*, 10(1), 2677. DOI: 10.1038/s41467-019-10442-3.
- Lundberg, S. M., & Lee, S. I. (2017). A unified approach to interpreting model predictions. *Advances in neural information processing systems*, 30. DOI: 10.48550/arXiv.1705.07874.
- Mahdizadeh Gharakhanlou, N., & Perez, L. (2022). Spatial prediction of current and future flood susceptibility: examining the implications of changing climates on flood susceptibility using machine learning models. *Entropy*, 24(11), 1630. DOI: 10.3390/e24111630.
- Meinshausen, M., Smith, S. J., Calvin, K., Daniel, J. S., Kainuma, M. L., Lamarque, J. F., ... & van Vuuren, D. P. (2011). The RCP greenhouse gas concentrations and their extensions from 1765 to 2300. *Climatic change*, 109, 213-241. DOI: 10.1007/s10584-011-0156-z.
- Météo-France, IPSL, CERFACS, CNRM-GAME. (2025). *DRIAS: French regionalized climate projections Dataset*. Retrieved from <https://www.drias-climat.fr/> on February 22, 2025.
- Montoya-Araque, E., Montoya-Noguera, S., Lopez-caballero, F., & Gatti, F. (2025). Numerical earthquake-induced landslide hazard assessment at regional scale in the Colombian Andes. *Soil Dynamics and Earthquake Engineering*. DOI: 10.1016/j.soildyn.2025.109370
- Moran, P. A. (1950). Notes on continuous stochastic phenomena. *Biometrika*, 37(1/2), 17-23. DOI: 10.2307/2332142.
- Mosavi, A., Ozturk, P., & Chau, K. W. (2018). Flood prediction using machine learning models: Literature review. *Water*, 10(11), 1536. DOI: 10.3390/w10111536.
- Nguyen, H. D. (2023). Spatial modeling of flood hazard using machine learning and GIS in Ha Tinh province, Vietnam. *Journal of Water and Climate Change*, 14(1), 200-222. DOI: 10.2166/wcc.2022.257.

Nguyen, H. D., Nguyen, Q. H., Dang, D. K., Van, C. P., Truong, Q. H., Pham, S. D., ... & Petrisor, A. I. (2024). A novel flood risk management approach based on future climate and land use change scenarios. *Science of The Total Environment*, 921, 171204. DOI: 10.1016/j.scitotenv.2024.171204.

Ongdas, N., Akiyanova, F., Karakulov, Y., Muratbayeva, A., & Zinabdin, N. (2020). Application of HEC-RAS (2D) for flood hazard maps generation for Yesil (Ishim) river in Kazakhstan. *Water*, 12(10), 2672. DOI: 10.3390/w12102672.

Özay, B., & Orhan, O. (2023). Flood susceptibility mapping by best-worst and logistic regression methods in Mersin, Turkey. *Environmental Science and Pollution Research*, 30(15), 45151-45170. DOI: 10.1007/s11356-023-25423-9.

Paszke, A., Gross, S., Massa, F., Lerer, A., Bradbury, J., Chanan, G., ... & Chintala, S. (2019). Pytorch: An imperative style, high-performance deep learning library. *Advances in neural information processing systems*, 32. DOI: 10.48550/arXiv.1912.01703.

Pawlewicz, M.J., Williams, A.J., Walden, S.M., Steinshouer, D.W., 2003, Generalized Geology of Europe including Turkey (geo4\_2l): U.S. Geological Survey data release, DOI: 10.5066/P9C8ZY5Q.

Pedregosa, F., Varoquaux, G., Gramfort, A., Michel, V., Thirion, B., Grisel, O., ... & Duchesnay, É. (2011). Scikit-learn: Machine learning in Python. *The Journal of machine Learning research*, 12, 2825-2830.

Pham, B. T., Jaafari, A., Van Phong, T., Yen, H. P. H., Tuyen, T. T., Van Luong, V., ... & Foong, L. K. (2021). Improved flood susceptibility mapping using a best first decision tree integrated with ensemble learning techniques. *Geoscience Frontiers*, 12(3), 101105. DOI: 10.1016/j.gsf.2020.11.003.

Pham, B. T., Phong, T. V., Nguyen, H. D., Qi, C., Al-Ansari, N., Amini, A., ... & Tien Bui, D. (2020). A comparative study of kernel logistic regression, radial basis function classifier, multinomial naïve bayes, and logistic model tree for flash flood susceptibility mapping. *Water*, 12(1), 239. DOI: 10.3390/w12010239.

Pradhan, B., Lee, S., Dikshit, A., & Kim, H. (2023). Spatial flood susceptibility mapping using an explainable artificial intelligence (XAI) model. *Geoscience Frontiers*, 14(6), 101625. DOI: 10.1016/j.gsf.2023.101625.

Prakash, N., & Manconi, A. (2021, July). Rapid Mapping of Landslides Triggered by the Storm Alex, October 2020. In *2021 IEEE International Geoscience and Remote Sensing Symposium IGARSS* (pp. 1808-1811). IEEE. DOI: 10.1109/IGARSS47720.2021.9553321.

Lam, R., Sanchez-Gonzalez, A., Willson, M., Wirnsberger, P., Fortunato, M., Alet, F., ... & Battaglia, P. (2023). Learning skillful medium-range global weather forecasting. *Science*, 382(6677), 1416-1421.

Rogers, J. S., Maneta, M. M., Sain, S. R., Madaus, L. E., & Hacker, J. P. (2025). The role of climate and population change in global flood exposure and vulnerability. *Nature Communications*, 16(1), 1287. DOI: 10.1038/s41467-025-56654-8.

Rudin, C. (2019). Stop explaining black box machine learning models for high stakes decisions and use interpretable models instead. *Nature Machine Intelligence*, 1(5), 206-215.

Rudra, R. R., & Sarkar, S. K. (2023). Artificial neural network for flood susceptibility mapping in Bangladesh. *Heliyon*, 9(6). DOI: 10.1016/j.heliyon.2023.e16459.

Saikh, N. I., & Mondal, P. (2023). Gis-based machine learning algorithm for flood susceptibility analysis in the Pagla river basin, Eastern India. *Natural Hazards Research*, 3(3), 420-436. DOI: 10.1016/j.nhres.2023.05.004.

Seabold, S., & Perktold, J. (2010). Statsmodels: econometric and statistical modeling with Python. *SciPy*, 7(1), 92-96.

Tansar, H., Babur, M., & Karnchanapaiboon, S. L. (2020). Flood inundation modeling and hazard assessment in Lower Ping River Basin using MIKE FLOOD. *Arabian Journal of Geosciences*, 13(18), 934. DOI: 10.1007/s12517-020-05891-w.

- Tehrany, M. S., Pradhan, B., & Jebur, M. N. (2014). Flood susceptibility mapping using a novel ensemble weights-of-evidence and support vector machine models in GIS. *Journal of Hydrology*, 512, 332-343. DOI: 10.1016/j.jhydrol.2014.03.008.
- Tende, C.-V. de. (2022, October 20). Storm Alex: Cerema present from the crisis management phase through to Reconstruction. Cerema. <https://www.cerema.fr/en/actualites/storm-alex-cerema-present-crisis-management-phase-through>. Accessed Mar 2025.
- Termeh, S. V. R., Kornejady, A., Pourghasemi, H. R., & Keesstra, S. (2018). Flood susceptibility mapping using novel ensembles of adaptive neuro fuzzy inference system and metaheuristic algorithms. *Science of the Total Environment*, 615, 438-451. DOI: 10.1016/j.scitotenv.2017.09.262.
- Toribio Diaz, C., & Vallhonrat Blanco, P. J. (2025). Resilient railways facing heavy rains (Report No. 5-25006E). UIC. <https://shop.uic.org/en/other-reports/14853-resilient-railways-facing-heavy-rains.html>
- Trenberth, K. E. (2011). Changes in precipitation with climate change. *Climate Research*, 47(1-2), 123-138. DOI: 10.3354/cr00953.
- Vaswani, A., Shazeer, N., Parmar, N., Uszkoreit, J., Jones, L., Gomez, A. N., ... & Polosukhin, I. (2017). Attention is all you need. *Advances in neural information processing systems*, 30.
- Van der Maaten, L., & Hinton, G. (2008). Visualizing data using t-SNE. *Journal of machine learning research*, 9(11).
- Veličković, P., Cucurull, G., Casanova, A., Romero, A., Lio, P., & Bengio, Y. (2017). Graph attention networks. *arXiv preprint arXiv:1710.10903*.
- Wang, Y., Fang, Z., Hong, H., Costache, R., & Tang, X. (2021). Flood susceptibility mapping by integrating frequency ratio and index of entropy with multilayer perceptron and classification and regression tree. *Journal of Environmental Management*, 289, 112449. DOI: 10.1016/j.jenvman.2021.112449.
- Wang, Y., Hong, H., Chen, W., Li, S., Panahi, M., Khosravi, K., ... & Costache, R. (2019). Flood susceptibility mapping in Dingnan County (China) using adaptive neuro-fuzzy inference system with biogeography based optimization and imperialistic competitive algorithm. *Journal of Environmental Management*, 247, 712-729. DOI: 10.1016/j.jenvman.2019.06.102.
- Wang, Z., Lyu, H., & Zhang, C. (2023). Pluvial flood susceptibility mapping for data-scarce urban areas using graph attention network and basic flood conditioning factors. *Geocarto International*, 38(1), 2275692. DOI: 10.1080/10106049.2023.2275692.
- Wang, Z., Lyu, H., & Zhang, C. (2024). Urban pluvial flood susceptibility mapping based on a novel explainable machine learning model with synchronous enhancement of fitting capability and explainability. *Journal of Hydrology*, 642, 131903. DOI: 10.1016/j.jhydrol.2024.131903.
- Widya, L. K., Rezaie, F., Lee, W., Lee, C. W., Nurwatik, N., & Lee, S. (2024). Flood susceptibility mapping of Cheongju, South Korea based on the integration of environmental factors using various machine learning approaches. *Journal of Environmental Management*, 364, 121291.
- Wing, O. E., Bates, P. D., Sampson, C. C., Smith, A. M., Johnson, K. A., & Erickson, T. A. (2017). Validation of a 30 m resolution flood hazard model of the conterminous United States. *Water Resources Research*, 53(9), 7968-7986. DOI: 10.1002/2017WR020917.
- Zhang, Q., He, Y., Zhang, Y., Lu, J., Zhang, L., Huo, T., ... & Zhang, Y. (2024). A Graph-Transformer method for landslide susceptibility mapping. *IEEE Journal of Selected Topics in Applied Earth Observations and Remote Sensing*. DOI: 10.1109/JSTARS.2024.3437751.
- Zhao, G., Pang, B., Xu, Z., Cui, L., Wang, J., Zuo, D., & Peng, D. (2021). Improving urban flood susceptibility mapping using transfer learning. *Journal of Hydrology*, 602, 126777. DOI: 10.1016/j.jhydrol.2021.126777.
- Zhao, G., Pang, B., Xu, Z., Peng, D., & Xu, L. (2019). Assessment of urban flood susceptibility using semi-supervised machine learning model. *Science of the Total Environment*, 659, 940-949. DOI: 10.1016/j.scitotenv.2018.12.217.

Zhou, J., Cui, G., Hu, S., Zhang, Z., Yang, C., Liu, Z., ... & Sun, M. (2020). Graph neural networks: A review of methods and applications. *AI open*, 1, 57-81.